J. Fluid Mech. (2005), *vol.* 525, *pp.* 115–159.
DOI: 10.1017/S0022112004002629 Printed in the United Kingdom

An experimental investigation of swirling jets

By HANZHUANG LIANG AND T. MAXWORTHY

Department of Aerospace and Mechanical Engineering, University of Southern California, CA 90089, USA

(Received 7 March 2003 and in revised form 30 September 2004)

The 'plug' flow emerging from a long rotating tube into a large stationary reservoir has been used in an experimental investigation of centrifugally unstable swirling jets. A moderate Reynolds number, $Re = 1000$, was studied extensively, and swirl numbers, S, the ratio of nozzle exit rotating speed to the mean mass axial velocity, were in the range 0–1.1. Four regimes were covered: non-swirling jets with $S = 0$, weakly swirling jets in the range $0 < S < S_{c1}$, strongly swirling jets before vortex breakdown with $S_{c1} < S < S_{c2}$, and stable vortex breakdown for $S > S_{c2}$, where $S_{c1} = 0.6$ and $S_{c2} = 0.88$.

Particular attention was paid to the dominant role of the underlying vortical flow structures and their dynamic evolution. Kelvin–Helmholtz (K–H) instability in the axial shear layer, generated by the axial velocity, leading to vortex ring formation, dominated non-swirling and weakly swirling jets. After the introduction of rotation, the combined axial and azimuthal shear layers became unstable to a modified form of K–H instability. For weak swirl, tilted vortex rings evolved downstream. For strongly swirling jets, vorticity in the azimuthal shear layer, formed by the azimuthal or swirl velocity, grew and became comparable with vorticity in the axial shear layer. The flow lost its axisymmetry and strong helical waves with $m = +2$ or $+3$ replaced vortex rings as the dominant vortex structure before vortex breakdown. After breakdown, strong helical waves with $m = +1$ and $+2$ coexisted, with $m = +1$ being dominant. Here, m is the azimuthal wavenumber, and the positive sign represents the counter-winding direction for helical waves. In the present experiments, the phase speed of each helical wave was the same as the rotation rate of the nozzle exit, in both direction and absolute value.

Based on a spectral study of the flow fields in natural, forced and transient experiments, we suggest that the helical wave $m = +2$ for strongly swirling jets before vortex breakdown and $m = +1$ after breakdown were self-excited/globally unstable, a behaviour identified as a super-critical Hopf bifurcation. Also it is suggested that the onset of the unstable global mode $m = +1$ after vortex breakdown was related to the existence of a region of local absolute instability in the wake region of the breakdown structure. This self-excited oscillation first dominated the inner shear layer between the central reverse flow and the conical jet, giving the breakdown the appearance of a spiral one, and then grew and incorporated the outer shear layer between the jet and the ambient fluid. After that, the wake region around the stagnation point served as the wave maker and imposed its frequency of oscillation on the whole flow. An attempt is made to reconcile these results with existing theory and experiments.

1. Introduction

Swirling jets represent one of a handful of basic flows that, while of great practical significance, allow the fundamental study of complex but generic dynamical processes and their interactions. They feature prominently in a variety of propulsion systems involving turbomachinery, such as jet engines and turbo-pumps. In combustion applications, their ability to create reverse flow regions near the jet nozzle has been exploited for the purpose of swirl-stabilizing the flame. The efficiency of chemical reactors and mixing devices is enhanced by making use of the faster spreading and more rapid mixing of the jet fluid with its surrounding by swirling compared with non-swirling jets. Atmospheric conditions can give rise to swirling flows with both wake and jet-like axial velocity profiles, e.g. tornados, dust devils and water-spouts. They are necessary feature of aircraft wake flows that have been known to cause damage to following aircraft.

In all of the above applications, the need for performance enhancement and optimization makes desirable an improved understanding of the interaction of the competing dynamical mechanisms that arise in swirling jets and govern their evolution. Their axial velocity profiles allow shear-induced instabilities similar to those encountered in non-swirling flows. However, the additional presence of swirl results in an azimuthal shear layer and centrifugal instability when the circulation decreases outwards. Finally, under certain conditions, i.e. when the swirl rate is high enough, swirling jets are known to produce vortex breakdown events. Improved understanding of these mechanisms and their mutual coupling is expected to pave the way for the development of passive and active flow control strategies employing sound, changes in nozzle geometry and motion, perhaps using micro machines.

The objectives of the present research are threefold. The first objective is to study the basic phenomenon of swirling jets, over a wide range of swirl number, S, at a moderate value of Reynolds number, Re. These dimensionless parameters are defined in § 2.2. By using high-resolution and real-time digital particle image velocimetry (DPIV), the velocity and vorticity fields have been precisely measured both on a central, vertical section of the jet and on horizontal slices at axial locations, x, from the nozzle exit $x = 0$ and $x = 0.5D$, D, $2D$ ($D = 3.82$ cm is the diameter of the nozzle exit). The second objective is to study the interaction and competition between different instability mechanisms, and identify the most unstable mode in the flow as S varies. Lastly, evidence is given regarding the convective/absolute, local/global, linear/nonlinear natures of the instabilities observed in swirling jets, aided by the spectral study of natural, forced and transient experiments.

An introduction to the basic physics of swirling flows is given, for example, by Gupta, Lilley & Syred (1984), while more advanced aspects, pertaining mostly to confined flows in slightly tapered tubes, were reviewed by Hall (1972), Leibovich (1978, 1983) and Escudier (1987). Breakdown in a uniform, jet-like, swirling approach flow is characterized by a transition to a wake-like velocity profile with a stagnation point followed by a reverse flow and/or highly turbulent region. Up to now it was thought that two forms of vortex breakdown exist as the *near-axisymmetric* and the *spiral* type, first described by Lambourne & Bryer (1961), although a number of other types have been observed, e.g. by Sarpkaya (1971). However, such a seemingly fundamental categorization is by no means certain and is open to further interpretation, as will be shown.

The design of swirl generators in practice has used one of the following principles for swirl generation: (i) adjustable vanes, e.g. Harvey (1962) and Panda & McLaughlin (1994), (ii) tangential inflow introduced into a pipe with an axial through-flow, e.g.

Chigier & Chervinsky (1967) and Escudier, Bornstein & Maxworthy (1982), (iii) fully developed pipe flow emerging from a long rotating tube with an exit contraction e.g. Billant, Chomaz & Huerre (1998) and Loiseleux & Chomaz (2003) or without a contraction as in the present work, and (iv) flow through a rotating, perforated plate, etc.

Before the late 1980s, the major focus of most experiments was to measure the time-mean flow fields and turbulent stresses, and expose some of the interesting characteristics of swirling jets, such as the displacement of the location of the maximum axial velocity from the axis, documenting the existence of a strong reverse flow near the centreline of the jet, the change in the magnitude of the velocity components with increase of the swirling velocity, and the high spreading rate of such jets. Only recently have researchers begun to pay more attention to the dominant role played by underlying vortical flow structures and their dynamical evolution, e.g. Panda & McLaughlin (1994) and the LadHyX group at the Ecole Polytechnique, Billant *et al.* (1998) and Loiseleux & Chomaz (2003).

Many theories of vortex breakdown have been proposed based on a number of different mechanisms. Ludwieg (1960, 1961, 1964) was the first to suggest that vortex breakdown might be a finite-amplitude manifestation of the linear instability of a swirling jet-like core flow in an annulus. Later, Brown & Lopez (1990) related the onset of vortex breakdown to the generation of negative azimuthal vorticity which depended initially on the viscous diffusion of the axial vorticity/swirl velocity in the vortex core. Mahesh (1996) presented a very simple criterion for vortex breakdown for both incompressible and compressible flows, in which the breakdown was assumed to happen when the axial pressure rise exceeded the upstream streamwise momentum flux.

Squire (1962) was the first to attempt to connect vortex breakdown with the theory of inertial wave propagation. Benjamin (1962) extended this concept and described vortex breakdown as a finite transition between super-critical upstream and sub-critical downstream states in an axisymmetric flow. Wang & Rusak (1997) found that the axisymmetric breakdown evolved as the result of the loss of stability of the columnar base flow when the swirl rate of the incoming flow exceeded a critical level, a result that is, as they state, strongly related to the critical state concept of Benjamin (1962). Further work on this problem can be found in Benjamin (1962), Leibovich (1970), Leibovich & Randall (1973), Randall & Leibovich (1973), Leibovich & Ma (1983), Kribus & Leibovich (1994), among others, to support the hypothesis that the axisymmetric-bubble-type breakdown phenomenon is associated with the development of large-amplitude, axially symmetric waves in a basic super-critical vortex flow. Experimental support can be found in Maxworthy, Hopfinger & Redekopp (1985), where propagating nonlinear axisymmetric solitons, with a large enough amplitude, were found to form co-rotating, counter-winding spiral tails as they propagated and had a morphology identical to that of a stationary vortex breakdown.

Escudier *et al.* (1982) presented arguments, based on their experimental observations, that there is a clear separation of the roles of flow criticality and flow stability. It was proposed that the state of criticality of the flow determines the basic, wake-like character of the downstream flow, and that the instability waves are a superimposed, but important, fine detail. The location of breakdown in the flow can be predicted by the transition from a super-critical to a sub-critical state to form an axisymmetric bubble. When this solitary wave or bubble reaches a certain critical amplitude, the wake-like velocity profile created in its interior becomes unstable to a discrete spectrum of spiral disturbances which grow rapidly, and it is these disturbances that

are responsible for the appearance of a breakdown dominated by spiral waves, so that often any sense of an axisymmetric wave is lost, although it still exists in the mean flow. This point of view and its extensions (see below) has been supported recently by the computations of Ruith *et al.* (2003).

During the past two decades, concepts of convective (CI)/absolute (AI), local/global and linear/nonlinear instabilities in open shear flows have been established by Fuchs, Ko & Bers (1981), Koch (1985), Chomaz, Huerre & Redekopp (1988), Monkewitz (1988), Huerre & Monkewitz (1990), Pier, Huerre & Chomaz (2001), Pier & Huerre (2001) and Huerre (2001), among many, and applied to swirling jet/wake shear layers, e.g. Martin & Meiburg (1994), Delbende, Chomaz & Huerre (1998), Loiseleux, Chomaz & Huerre (1998), Lim & Redekopp (1998), Olendraru *et al.* (1999), Loiseleux, Delbende & Huerre (2000), Yin *et al.* (2000), Olendraru & Sellier (2002), Gallaire & Chomaz (2003*a*, *b*) and Ruith *et al.* (2003). AI was found to be significantly enhanced by the presence of the swirl in linear instability analysis of shear layers in centrifugally stable and unstable jets and wakes. It should be noted that the following review is given only for rotating free jets and wakes which have no external swirl or axial flow.

It appears, based on the major differences that have been observed, that one can divide existing studies into two groups depending on subtle differences in the inlet velocity profiles. Some inlet profiles had axial and azimuthal shear layers that intimately overlapped at a radius close to or coincident with the edge of the inlet, e.g. in calculations by Martin & Meiburg (1994), Lim & Redekopp (1998), Loiseleux, Chomaz & Huerre (1998), Loiseleux, Delbende & Huerre (2000), Gallaire & Chomaz (2003*a*), Ruith *et al.* (2003) and also in the present experiments. For centrifugally unstable jets, AI was triggered via the axisymmetric mode $m = 0$ and then co-rotating counter-winding helical waves appeared as the swirl difference increased, e.g. $m = +1$ to $+5$ with $k > 0$ was observed by Loiseleux *et al.* (2000) in calculations based on an idealized swirl velocity profile with plug flow considered earlier by Martin & Meiburg (1994) and Lim & Redekopp (1998). For the case of centrifugally destabilizing wakes, counter-rotating co-winding helical waves, e.g. $m = +1$ to $+8$ † with k positive for a screened Rankine vortex with plug flow studied by Gallaire & Chomaz (2003*a*), were found to be the most unstable modes and absolutely unstable (AU) as the swirl difference increased. On the other hand centrifugally stable swirl differences for jets led to AI via counter-rotating and co-winding helical waves, e.g. $m = -1$ to -5 for Rankine vortex with plug flow calculated by Loiseleux *et al.* (1998). And centrifugally stable wakes were calculated to become AU via co-rotating counter-winding helical waves, e.g. $m = -1$ to -5 also for Rankine vortex with plug flow by Loiseleux *et al.* (1998).

For instabilities in the above theoretical studies on centrifugally unstable jets and centrifugally stable wakes, as well as in the present experimental investigation for strongly swirling jets before and after vortex breakdown, the most absolutely unstable modes observed were more aligned with the local mean vortex line. The Rayleigh centrifugal instability is not relevant for these counter-winding helical waves but rather a combination or competition of the Kelvin–Helmholtz (K–H) instability and the generalized centrifugal instability of Ludwieg (1960, 1961, 1964) and Leibovich &

† When referring to the rotating jet or wake studies, the sign of m defined in experimental investigations is based on the positive streamwise direction at the inlet both before and after breakdown, whereas in many theoretical studies, the sign of m is reversed for wakes, since the direction of the base flow is defined by the sign of the axial velocity difference. A detailed argument can be found in Gallaire & Chomaz (2003*b*).

Stewartson (1983). For swirling free jets after breakdown, the centrifugal instability still exists between the jet and the stationary ambient, a region named the outer shear layer in the present paper, but the wake region within the bubble breakdown structure, named the inner shear layer, is in solid-body rotation and thus locally centrifugally stable. The absolute nature of the counter-winding helix that is well known in the bubble wake region, defined as $m = +1$ in experiments and $m = -1$ in theories, can be modelled in first approximation by the Batchelor modes as in Delbende *et al.* (1998), Olendraru *et al.* (1999) and Olendraru & Sellier (2002), but the physical underlying mechanisms remain to be identified.

In the second major group of studies, inlet velocity profiles with the peak azimuthal vorticity in the axial shear layer, due to the axial flow, were substantially displaced from the location of the maximum axial vorticity in the azimuthal shear layer, due to the swirl flow. For example, in the theoretical studies of Gallaire & Chomaz (2003*b*), and experiments by the LadHyx group, Billant *et al.* (1998) and Loiseleux & Chomaz (2003), the axial shear-layer instability covered the range from approximately $r = 0.9R$ to $1.1R$ while the major part of the azimuthal shear layer covered the appoximate range from $r = 0.5R$ to $1.1R$. In the calculation by Gallaire & Chomaz (2003*b*), a counter-rotating co-winding helical wave, $m = -2$, was found as the only AU mode for centrifugally unstable jets while centrifugally unstable wakes became AU via co-rotating counter-winding spirals, $m = -1$ to -6, as the swirl differences increased. In their experimental investigation of swirling free jets, Billant *et al.* (1998) observed counter-rotating co-winding helical waves, $m = -2$ and -3, before breakdown which agrees with calculations for centrifugally unstable jets by Gallaire & Chomaz (2003*b*). These co-winding helical waves are similar to phenomena found in Taylor–Couette flow with axial flow where the centrifugally induced pressure gradient is able to stretch, bend and reorient the mean vortex lines (Ludwieg 1961, 1964). In their experiments, Billant *et al.* (1998) also observed co-rotating counter-winding spirals for flows after breakdown. These counter-winding modes are similar to those found to be the most absolutely unstable after breakdown in the present experiments and for centrifugally stable wakes in calculations by Loiseleux *et al.* (1998) and Ruith *et al.* (2003).

Globally unstable behaviour has been related to the local instability of spatially developing flows by the argument that in a linear system the bifurcation to a self-excited global mode may be possible only after a sufficiently large area of the flow has become absolutely unstable. Here the frequency of oscillation was determined by that of the linear problem at the transition from convective to absolute instability (see e.g. Koch 1985). More recently, this linear criterion has been found to be true even for the nonlinear 'steep-mode' of Pier *et al.* (2001) and Pier & Huerre (2001) (Huerre, private communication). This point of view updates the description of the phenomena presented earlier by Escudier *et al.* (1982) and Maxworthy *et al.* (1985). In this interpretation, as before, the axisymmetric breakdown is considered as a super-critical to sub-critical transition. When the solitary wave or bubble reaches a certain critical amplitude, with an AU region that is large enough, the flow becomes globally unstable to asymmetric instabilities. These helical oscillations can become self-excited and rapidly overwhelm the whole flow and the bubble transitions to one of the spiral type. For swirl numbers well above critical, the global instability may be controlled by nonlinearity, and the globally unstable mode may appear as soon as there exists a point of AI, in the present case most probably around the stagnation point after breakdown. As noted above, this kind of nonlinear oscillation is called a 'steep mode' in the theory of Pier *et al.* (2001) and Pier & Huerre (2001).

Two classes of experiments are required, according to the theories reviewed by Huerre & Monkewitz (1990), to decide if an observed oscillation is the consequence of a self-excited/globally unstable mode, and in the present experiments an attempt is made to follow these prescriptions. The first class contains 'easy' experiments, which examine the steady-periodic behaviour of the flow and include: (i) a study of spectral distributions to determine the presence of limit-cycle behaviour; (ii) determining if the saturation amplitude versus the control parameter (such as the swirl number in the present work with Reynolds number fixed) is consistent with dictates of the Landau equation and with indications of a super-critical Hopf bifurcation; (iii) obtaining the relationship between the flow response and the amplitude of steady-periodic low-level external forcing at the suspected global frequency/mode number to identify whether the flow is self-excited or just convectively unstable. These 'easy' experiments provide only supporting evidence. A more positive proof that an unstable global mode has emerged can only be furnished by including a class of 'hard' experiments, namely transient analyses of the bifurcation.

2. Experimental setup and procedures

2.1. *Apparatus*

In order to supplement and verify the theoretic analyses and numerical computations discussed above, an experimental program has been designed which can cover the range of conditions of interest. This was accomplished in the apparatus shown as an assembly drawing in figure 1. It consisted of a vertical swirling jet emerging into a large stationary test tank. The test tank was designed to rotate independently; however, this feature was not used in the present study. Tap water was used and was always filtered before adding and mixing the particles used to track the flow and record digital images. The water exiting the test tank was collected in a large reservoir and then pumped to a five-gallon reservoir, which was suspended above the rotating nozzle assembly to filter oscillations of the flow rate and provide a constant-head inflow. The flow rate was controlled by several valves underneath the test tank and measured by a flow meter located before the rotating nozzle assembly. The water was recycled to maintain clarity and to save particles. Before the experiments, the water was stored for at least one day to eliminate air bubbles and to reach a uniform temperature.

The basic rotating nozzle subsystem is shown in more detail in figure 2. It consisted of a rotating manifold containing a honeycomb of straws that both smoothed the incoming flow and allowed it to be brought to a solid-body rotation within a short axial distance. The swirl velocity component was imparted to the jet by means of a motor and two concentric cylinders. The outer cylinder was fixed to the top of the test tank and the inner rotating cylinder was held in the outer cylinder by radial bearings, and rotated smoothly around the axis of the system. The rotation rate of the pipe was maintained constant by a motor with feed-back servo control. The swirling jet ended in a straight nozzle attached to the inner cylinder. Contracting nozzles have been used in most experiments to produce a laminar and uniform non-swirling jet. However experiments have also shown that the fully developed swirling jets coming from such a nozzle, see e.g. Billant *et al.* (1998), have a central over-shoot in the axial velocity within the vortex core. Under these circumstances the inflow conditions were hard to control since each rotation rate gave a different axial velocity profile, which must certainly affect the swirl number at which vortex breakdown was generated. Because of this a smooth but non-contracting nozzle of diameter $D = 1.5$ in. was used

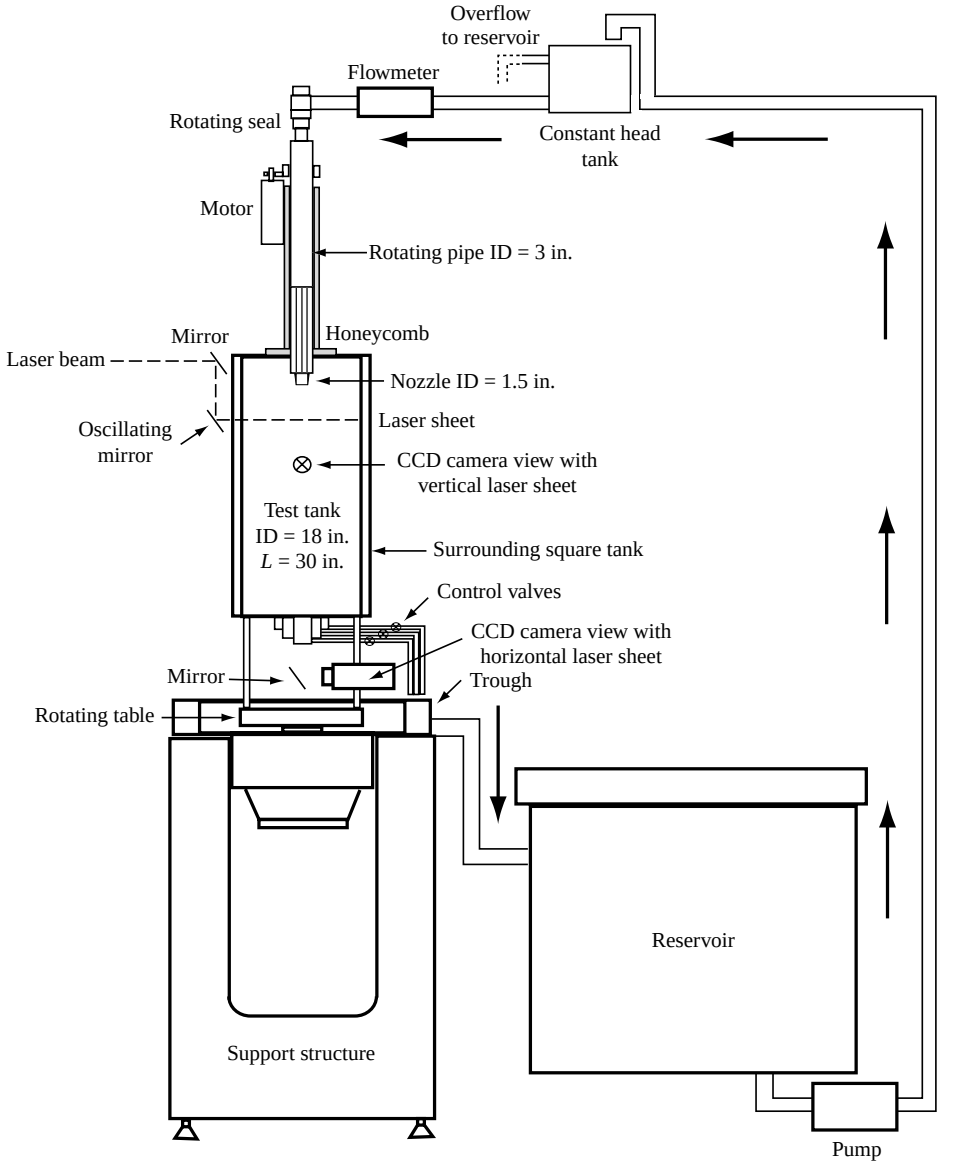

FIGURE 1. Sketch of the experiment setup.

in the present experiments, even though it caused some slight non-uniformity and a higher level of turbulence in the exit flow. In the first nozzle design, producing flow A (figure 2*a*), the slight mismatch at the transition from the honeycomb to the nozzle apparently caused a small over-shoot at the jet shoulder and higher turbulence level in the shear layer, as documented in detail in Liang (2003) and Liang & Maxworthy (2005). However this effect was suppressed by using an inner pipe with the same diameter as the nozzle and straws with smaller inner diameter. The steel mesh was removed from underneath the honeycomb, since it sometimes trapped air bubbles. In this way, an improved laminar free-swirling jet, flow B (figure 2*b*), was generated and used to analyse in detail the spatio-temporal development of the instabilities, while

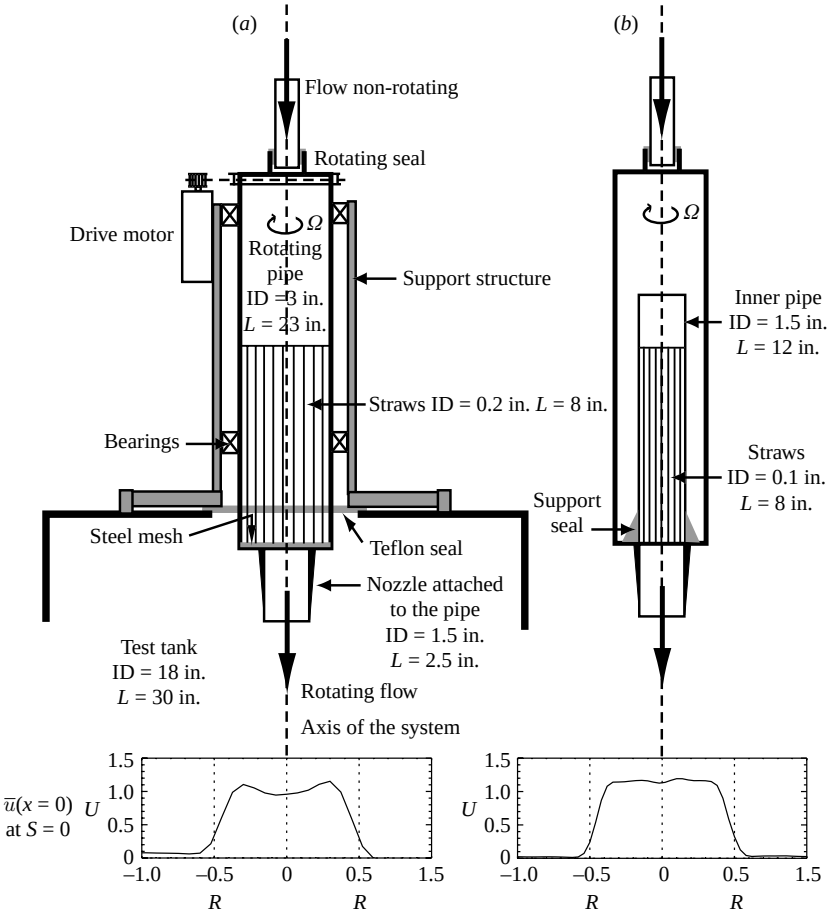

FIGURE 2. Details of the nozzle assembly and the dimensionless mean axial velocity of the non-swirling flow generated at the nozzle exit $x = 0$: (*a*) flow A, (*b*) flow B.

flow A was used for preliminary visualization and mean flow measurements (also see Liang & Maxworthy 2005).

The test tank was a large, transparent circular cylinder. A square tank surrounded the cylindrical tank and was filled with water to eliminate optical distortion. Both tanks were concentric with the upper nozzle assembly.

As shown in the basic configuration (figure 2), the rotating element was designed to produce a jet with an initially uniform axial velocity and solid-body swirl or azimuthal velocity, both with outer shear layers to bring the velocity to that of the outer stationary flow. It should be emphasized that the relatively large size of the test tank made the jet a nearly free one and the exit azimuthal shear layer was centrifugally unstable by design when the jet rotated.

2.2. *Control parameters*

There are two independent control parameters for the swirling jet, flow rate and rotation rate of the nozzle, which can be expressed in terms of true non-dimensional independent parameters, Reynolds number Re and swirl number S. The Reynolds number is defined as

$$Re = UD/\nu \tag{2.1}$$

where the mean mass axial velocity, $U = Q/\pi R^2$, is the flow rate Q divided by cross-sectional area of the nozzle exit, and $D = 3.82\,\text{cm}$ is the diameter of the nozzle exit, R is its radius, $D/2$, and ν is the coefficient of kinematic viscosity of water. The swirl number is defined as the ratio of the azimuthal velocity of the nozzle exit to U (also known as the Taylor or inverse Rossby number), i.e.

$$S = \Omega R/U \tag{2.2}$$

Here Ω (s^{-1}) is the rotation rate of the nozzle assembly. In the present investigation, a moderate Reynolds number, $Re = 1000 \pm 50$, i.e. $U = 2.60$–$2.88\ \text{cm}\,\text{s}^{-1}$, was chosen for most studies, and a broad range of swirl number, $S = 0$–1.1, was covered to observe the phenomena of interest, e.g. vortex shedding, pairing, spiralling and breakdown. Note that these are true independent parameters since they do not depend on any measured values in the jet, as has been the case in some studies.

2.3. *Instrumentation, data acquisition and processing*

Basically there are two ways to measure flow field velocities. One is by inserting probes into the flow but these certainly change the profiles when the flow is rotating and can support inertial waves. Examples are hot-wire/film anemometers and Pitot probes, which are thus undesirable for the measurement of swirling flows. Another technique is to record the flow traced by particles and then calculate the velocity fields, using either digital particle image velocimetry (DPIV) or laser-Doppler velocimetry. DPIV is cheaper and more efficient, since it can record data over a slice of the whole flow instead of one point at a time. DPIV is known to work for relatively slow flows, such as the present swirling flow with a moderate Reynolds number 1000 and swirl numbers not much larger than one.

In the present experiments, the light source was a 5 W argon-ion laser. The laser sheet was generated by a function-generator-controlled mirror continuously oscillating at 200 Hz, which provided an effectively instantaneous pulse containing a high frequency scan. By changing the oscillation direction of the mirror, a laser sheet perpendicular to the axis of the jet or a sheet that contains the jet axis could be obtained. Reflections, the glow from dirty water and the tank structure could seriously reduce the image quality. So the water used in the experiment was carefully cleaned, the test tank was covered by black contact paper except for the visualization zone, and all lights in the laboratory were turned off when recording data. Fluorescein was injected into the flow at the rotating seal to visualize the flow and was illuminated by the laser sheet. In this case, to maintain high photographic contrast, the water from the test tank was not recycled. Still pictures and video recordings were taken.

In our laboratory we have developed a high-resolution DPIV system, called correlation image velocimetry (CIV) (Fincham & Spedding 1997). By using a series of sophisticated checking routines and by optimizing the particle size, brightness and seeding density, time between frames, search area and correlation boxes, it is possible to obtain velocity vectors accurate to approximately 1% and vorticity to approximately 3% using a video-based system with a standard 768×484 CCD array operating at the maximum of 30 frame s^{-1}. The Plyolite particles chosen in our experiment had good light reflection properties. They had a round shape, mostly of diameter 50 μm, and were approximately neutrally buoyant in the fluid, with a specific gravity of 1.03–1.05. A number of particles with size in the range 30–100 μm were added and the particle density in the fluid was high. This wide distribution of particle sizes improved performance, as each local image pattern had a better chance of being unique. It should be noted that the axial position, $x = 0$, for both vertical and

horizontal slices, was actually located close to the nozzle at $x = 3$–5 mm, to exclude the intense reflection from the nozzle when the digital images were recorded. But for convenience, it is still denoted as $x = 0$ in this paper if not otherwise stated.

A Pulnix TM 745 interline-transfer, black and white CCD video camera was used to take the digitized images. These images were captured on a PIII PC fitted with an ITI PC-Vision frame grabber board, which was then used to compute velocity fields of the flow, using an algorithm provided by Professors A. Fincham and G. Spedding. This video camera could also capture and save analogue video when connected to a VCR.

2.4. *Calculation of flow quantities from CIV data*

Time-averaged flow fields in horizontal slices were assumed to be axisymmetric due to the circular geometry of the jet and the test tank. For example when calculating the instantaneous circulation on horizontal slices of the jet, integration took place along a circle at each radius, i.e.

$$\Gamma = wr = \int_0^{2\pi} w(x, r, \theta) r \, \mathrm{d}\theta = \sum_{k=0}^{K-1} w(x, r, k\Delta\theta) r \, \Delta\theta$$

where $\Delta\theta = 2\pi/K$. Values are non-dimensionalized using: axial distance from the nozzle exit, giving x/D; radius, giving r/R; axial velocity, giving u/U; radial velocity, giving v/U; circulation, giving $\Gamma/(2\pi\Omega R^2)$; and azimuthal velocity, giving $w/(\Omega R)$, where the velocity vector $\boldsymbol{u} = (u, v, w)$ in the cylindrical coordinate system (x, r, θ).

For time-averaging flow fields on vertical or horizontal slices of the jet, 120 flow field realizations, $N = 120$, were used with the time step $\Delta t \approx 0.4$ s between them. The sampling rate, $1/0.4\,\mathrm{s}^{-1}$, was about eleven times faster than the rotation rate of the nozzle when $S = 1$ and $Re = 1000$, i.e. $\Omega = 1/4.38$ revolution s^{-1}, and the recording time, 48 s, covered about eleven full revolutions under this condition. Again using the circulation as an example, the time-averaged mean quantity is then given by

$$\overline{\Gamma} = \frac{1}{T} \int_0^T \Gamma(t) \, \mathrm{d}t = \frac{1}{N} \sum_{n=0}^{N-1} \Gamma(n) \Delta t$$

with the root-mean-square (RMS) value of the corresponding fluctuation defined as

$$\Gamma' = (\overline{[\Gamma(t) - \overline{\Gamma}]^2})^{1/2} = \left(\frac{1}{N-1} \sum_{n=0}^{N-1} [\Gamma(n) - \overline{\Gamma}]^2 \right)^{1/2}.$$

The azimuthal vorticity of figure 6, for example, was calculated from the instantaneous axial and radial velocities on a vertical slice of the jet:

$$\omega_\theta(x, r) = \frac{\partial u}{\partial r} - \frac{\partial v}{\partial x} = \frac{u(x, r) - u(x, r - \Delta r)}{\Delta r} - \frac{v(x, r) - v(x - \Delta x, r)}{\Delta x}$$

where Δx and Δr are the axial and radial spatial step of the meshed velocity fields calculated by CIV.

3. Flow visualization

Flow visualization studies were undertaken on model flow A. For most studies, a moderate Reynolds number $Re = 1000$ was chosen with a wide range of swirl number $S = 0$–1.1 to cover four regimes: non-swirling jet with $S = 0$, weakly swirling jets in the

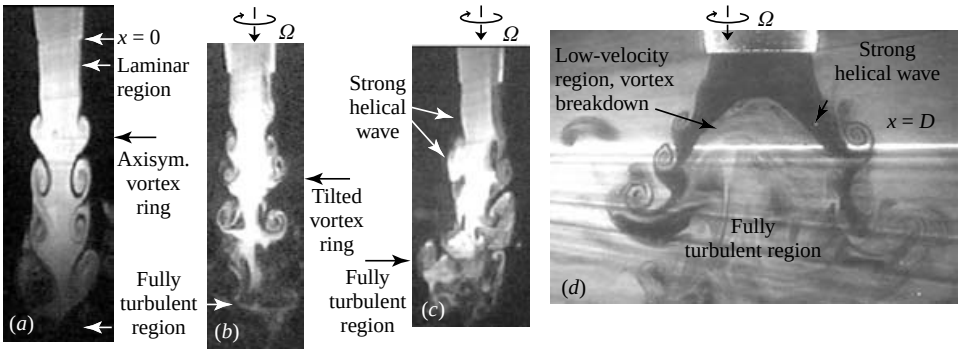

FIGURE 3. Instantaneous photographs with laser sheet illumination of a central, vertical slice of the jets: (*a*) $S = 0$, (*b*) $S = 0.44$, (*c*) $S = 0.80$, (*d*) $S = 1.03$. $Re = 1000$, i.e. $U = 2.74$ cm s^{-1} for flow A.

range $0 < S < 0.6$, strongly swirling jets before vortex breakdown with $0.6 < S < 0.88$, and stable vortex breakdown for $S > 0.88$.

3.1. *Before breakdown*

Without swirl ($\Omega = 0$, i.e. $S = 0$), the jet evolved downstream, while Kelvin–Helmholtz instability, resulting from the axial velocity difference between the jet and the ambient fluid, led to the tendency for the laminar shear layer shed from the nozzle exit to roll up into discrete and axisymmetric vortex rings at $x \approx 2D$ (figure 3*a*). These vortex rings grew in the streamwise direction while propagating at about half of the velocity of the mean flow. Vortex pairing was observed further downstream and accounted for most of the spreading of the jet (see e.g. Browand & Laufer 1977). The local vortex shedding frequency decreased in the positive axial direction until $x \geqslant 5D$, where the flow reached a fully turbulent state downstream and distinct vortices could no longer be observed. The region between the nozzle exit and the first roll-up position, $0 \leqslant x \leqslant 2D$, was called the laminar region, where the amplitudes of instability waves were relatively small. Viewed from horizontal slices, the diameter of the jet increased as a vortex ring approached from upstream, and then decreased as the ring left this axial location and propagated further downstream. A secondary azimuthal instability was visible in horizontal slices downstream of the laminar region, as a vortex ring passed through it.

With Re fixed and the swirl rate increasing slowly from zero, streaklines in the jet became helical due to the solid-body rotation of the flow. The rotation direction of the mean flow was from right to left on the vertical slice of the jet in figure 3(*b–d*), and clockwise on horizontal slices if viewed from upstream in figure 4(*b–d*). Vortex rings maintained their axial symmetry upstream and became tilted downstream. An azimuthal shear-layer instability evolved between the rotating jet and the stationary ambient fluid. This type of vortex rolled up in a direction opposite to that of the solid-body rotation, while it co-rotated with the jet (figure 4*a*). These instability vortices were only visible in horizontal cross-sections and were rapidly convected away by the mean flow. Viewed as horizontal slices downstream of the laminar region, these vortices grew stronger when a vortex ring passed by from upstream, and became weak or even disappeared as the vortex ring propagated further downstream, i.e. a similar behaviour to the secondary azimuthal instability found in the vortex rings in a non-swirling jet. For weakly swirling jets, the axial shear-layer instability led to vortex rings that still dominated the flow, and the vortices due to the azimuthal shear layer

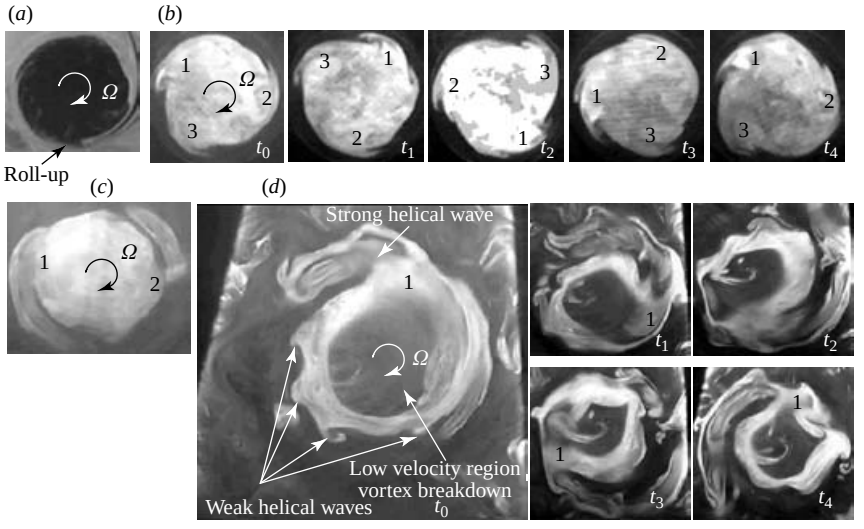

FIGURE 4. Instantaneous photographs of a horizontal slice of the jets: (*a*) $S = 0.44$ at $x = D$, (*b*) $S = 0.63$ at $x = 0.5D$, (*c*) $S = 1$ at $x = 0.5D$, (*d*) $S = 0.90$ at $x = 1D$. $Re = 1000$. In (*b*) and (*d*), the trace of helical waves, marked as '1', '2' and '3', is shown for one revolution, e.g. $t_0 = 0$, $t_1 = 0.25T$, $t_2 = 0.5T$, $t_3 = 0.75T$ and $t_4 = T$, where T is the time for the nozzle to rotate one full turn.

were considered to be secondary. Small-scale random turbulence grew in the shear layer and made the flow visibly and measurably more turbulent than the non-swirling jet.

Swirl expanded the mixing region so that the jet spread faster than a non-swirling one (see § 4.1.1), and the entrainment of ambient fluid was higher. The laminar region became shorter at larger swirl number, and the fully turbulent region was located further upstream, e.g. at $x \approx 3D$ for $S = 0.44$.

As S increased further, the flow became more complicated and irregular (figure 3*c*), and vortices associated with instability of the azimuthal shear layer grew stronger (figure 4*b*). When S was above the first critical value, i.e. $S_{c1} \approx 0.60$, the shear layer lost its axial symmetry, and helical waves grew and replaced vortex rings to become the dominant vortex structure. The breakup of the flow symmetry from the origin, and the existence and evolution of intense vortex spirals, were detected first from the study of the azimuthal vorticity contours calculated from the velocity field on the vertical cross-section of the jet (see § 3.3.1). They were confirmed by careful observation of the dyed jet. More details can be found in § 3.3 and Liang (2003). The vortex core was relatively stable and laminar close to the nozzle exit. After that, the flow rapidly became fully turbulent at $x \geqslant 2D$. At the same time, small-scale vortices, e.g. random turbulence and weak helical waves, grew and made the larger-scale vortices irregular and unorganized. This competition and interaction of instabilities made the vortex spiral very unstable and hard to visualize, especially as the flow approached the condition of vortex breakdown.

3.2. *Vortex breakdown*

Vortex breakdown has been defined as an abrupt flow transition with a free stagnation point/region on the axis followed by a reverse flow and a fully turbulent region (figures 3*d* and 4*d*). The critical swirl number for breakdown to appear and stabilize

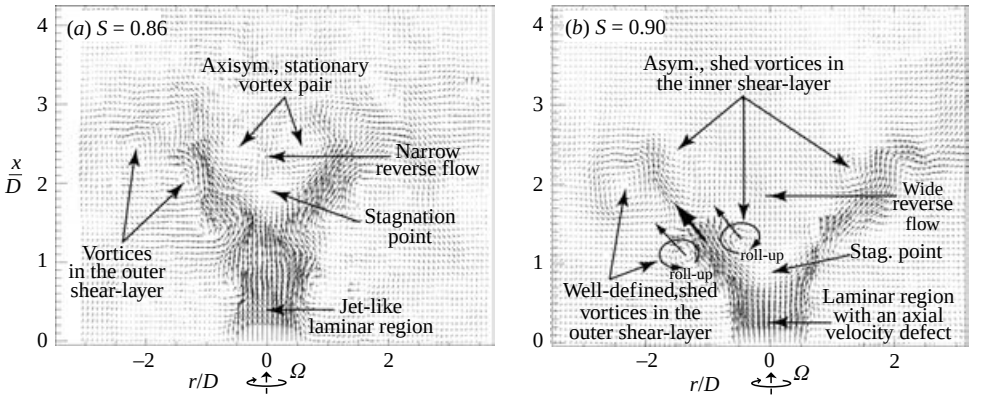

FIGURE 5. Instantaneous velocity vector images on a central, vertical slice of jets after breakdown. (*a*) At $S = 0.86$, the vortex pair that defines the interior of the incipient vortex breakdown is axisymmetric, stationary and of large size with a narrow reverse flow between them. (*b*) At $S = 0.90$, vortices are asymmetrically located, shed downstream in time and are smaller with a wide reverse flow in between. For larger S, the jet spreads more rapidly with breakdown located closer to the nozzle exit. $Re = 1000$.

in the flow is $S_{c2} = 0.88$ at $Re = 1000$ in the present experiments. At S between 0.86 and 0.88, vortex breakdown was unsteady and oscillated axially over a fairly wide range of amplitude (see Liang 2003 and Liang & Maxworthy 2005). The stagnation point/region existed far downstream, $x \leqslant 4D$, for $S = 0.83$–0.86, but no well-organized breakdown structure was formed at these early stages.

After the vortex breakdown had stabilized, the flow became regular with fewer small-scale vortices in the shear layer. The vortex breakdown and strong helical waves in the shear layer were well defined and clearly visible (figures 3*d* and 4*d*). The jet spread much faster (see § 4.1.1) and the entrainment rate of ambient fluid was high. This highly mixed region moved closer to the nozzle exit as S increased further.

Details of the inner structure of vortex breakdown for various degrees of swirl are demonstrated by instantaneous velocity vector images recorded on vertical cross-sections of jets (figure 5*a*, *b*) for flow A. At $S = 0.86$, downstream of the stagnation point, there was what appeared to be a near-axisymmetric and stationary vortex ring, $m = 0$, i.e. a counter-rotating vortex pair when viewed as a vertical slice of the jet in figure 5(*a*). At a larger value of S, e.g. 0.9, two vortices were shed together and propagated along the conical shear layer, as in the lower left-hand side of figure 5(*b*). These were manifestations of counter-winding helical vortices.

The near-axisymmetric breakdown was only observed at swirl numbers just before the stable vortex breakdown appeared, i.e. in the range $S = 0.86$–0.88. It had a smaller divergence angle and was located further downstream. The flow upstream was still jet-like. This flow type was unsteady, and the bubble frequently disappeared and then reappeared. At larger swirl number, i.e. $S \geqslant 0.88$, the asymmetric spiral structure became well-organized and was located closer to the nozzle exit. The flow developed a central velocity defect at the nozzle exit, see example figure 8, i.e. the upstream effect of breakdown propagated into the nozzle (see § 4.2.1).

The conical axial shear layer became double-sided as vortex breakdown stabilized close to the nozzle exit (figures 5*b* and 6). The inner (wake) shear layer, between the reverse flow and the conical jet, was centrifugally stable, and its vortex structure defined the type of spiral vortex breakdown; while the outer (jet) shear layer, between

the spreading jet and ambient fluid, was where the centrifugal instability existed. In these two shear layers, the helical vortex lines were aligned, but with the axial and the azimuthal vorticity pointing in opposite directions.

3.3. *Details of vortex spiral morphology*

3.3.1. *Spiral configuration*

Before discussing the morphology of the vortex field in detail it is necessary to define precisely the meaning of each of the words and symbols used. In the literature on the subject this has not often been done and this omission has caused great difficulty in interpreting many of the previous results. Following Martin & Meiburg (1994), the phase function of the disturbance at a fixed time is defined as $(kx + m\theta)$, where x is in the direction of the mean axial flow and θ increases in the direction of the basic rotation. With these definitions a mode with m positive $(+m)$ has a line of constant phase with a sense of winding in the opposite direction to the basic rotation and is called counter-winding, i.e. with increasing x a point on a line of constant phase moves in an azimuthal direction opposite to that of the basic rotation. Conversely, a helix with m negative $(-m)$ has a sense of winding in the same direction as the rotation and is called co-winding. Additionally, the disturbance is said to be co-rotating if a point on a line of constant phase rotates in the same direction as the underlying rotation and counter-rotating if it rotates in the opposite direction. It should be noted that in many theoretical studies, the sign of m is reversed for wakes, since the direction of the base axial flow is defined by the axial velocity difference. A detailed discussion can be found in Gallaire & Chomaz (2003*b*).

Also, one useful, physically based, way to discuss the results that follow is to note that in the present experiments, the lines of constant phase and the finite-amplitude vortex structures that evolve were always aligned with the mean vortex lines of the basic flow field. This result is physically reasonable and is confirmed by some available theories, e.g. Martin & Meiburg (1994), and experimental observations, e.g. for swirling free jets after breakdown by Billant *et al.* (1998). Contradiction can also be found in theories, e.g. Gallaire & Chomaz (2003*b*), and experiments, e.g. for flows before breakdown in Billant *et al.* (1998).

Vortex spirals observed in the present experimental investigation co-rotated with the jet, and their phase speed was the same as the rotation rate of the nozzle exit, Ω, as shown in figure 4(*b*, *d*). But their inclination, or their sense of winding, was in the direction opposite to that of the mean swirl. In our present convention, these are designated as m positive modes. Figure 6(*a*) shows a sample of the spatial evolution of vortices calculated from DPIV velocity fields as $m = +2$ at $S = 1.03$. Figures similar to this for different values of S can be found in Liang (2003) and Liang & Maxworthy (2005). Here for clarity, vortex spirals were reconstructed only in the outer shear layer. The number of spirals in the flow equalled the number of vortices that appeared at a fixed point on one side of the jet, during one revolution, on the vertical cross-section. This process is illustrated on figure 6(*b*) where one revolution is divided into 11 intervals and the appearance of a new vortex at a fixed location near the nozzle exit initiated a new revolution. This vortex was then followed at each interval as it propagated downstream and thus the vortex helix could be reconstructed.

3.3.2. *The most unstable modes*

From the present investigation, the most unstable mode in the shear layer was $m = 0$ for non-swirling and weakly swirling jets with $S < S_{c1} \approx 0.6$, and large-scale vortex rings dominated the shear layer. When S was increased above S_{c1}, vortex spirals

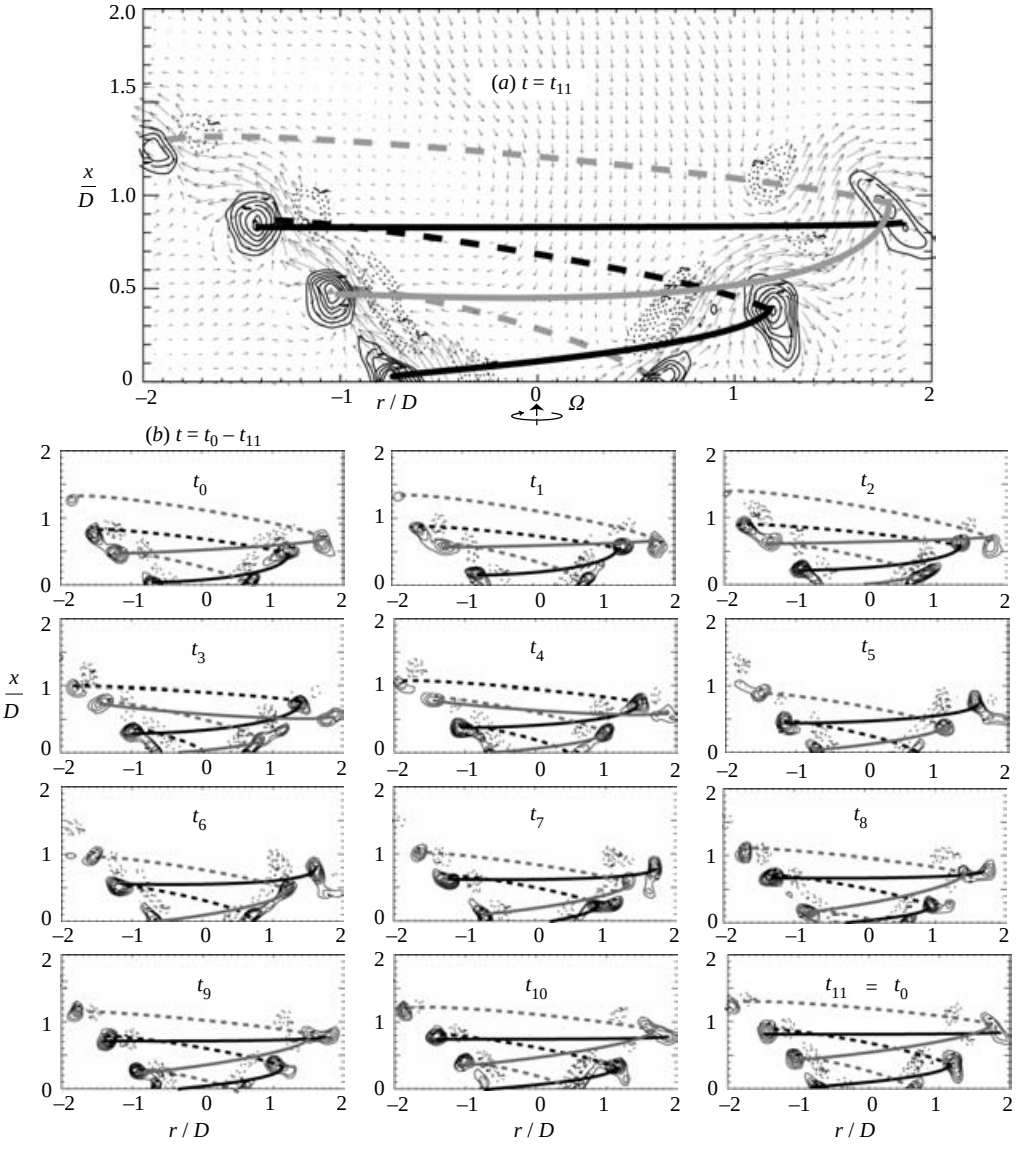

FIGURE 6. Spatial and temporal evolution of the vortex spirals, $m = +2$ at $S = 1.03$, $Re = 967$, i.e. $U = 2.65$ cm s^{-1}. One revolution is divided into eleven intervals and then each vortex is followed. (*a*) At t_{11}, the vorticity contours are superimposed on the velocity vector image, and are marked as solid contours in the outer shear layer and dotted contours in the inner shear layer. Vortex spirals were reconstructed only in the outer shear layer as a guide to the eye and shown in black and grey, being solid if nearer to the viewer and dashed if further away. (*b*) During one revolution t_0–t_{11}, two vortices appear on the left side of nozzle exit, one at t_0 and the other at t_5, which belong to the black and grey spirals respectively.

evolved and became the dominate vortex structure in the flow. The most unstable modes were $m = +2$ or $+3$ before breakdown, i.e. $S_{c1} < S < S_{c2} = 0.88$. Examples are shown in figure 4(*b*) e.g. $m = +3$ at $S = 0.63$ from a horizontal cross-section $x = 0.5D$. After vortex breakdown $S \geqslant S_{c2}$, the spiral structure became regular and clearly visible. As vortex breakdown reached its steady state, spirals $m = +1$, $+2$ coexisted. For most

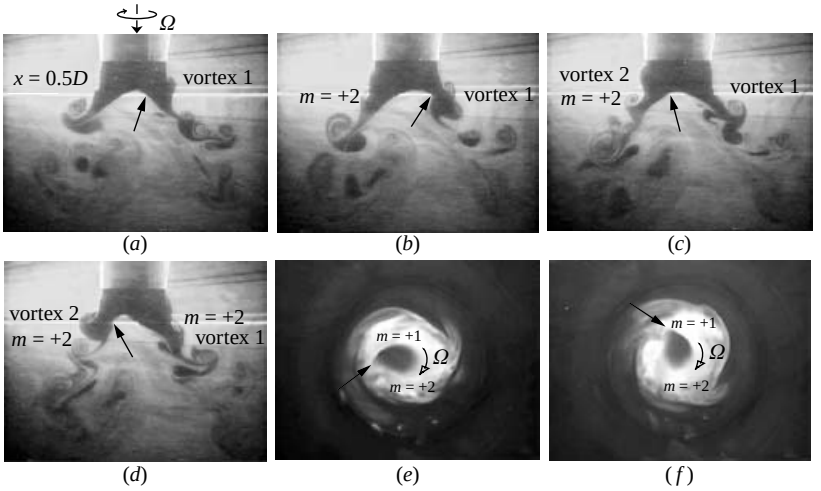

FIGURE 7. The movement of the stagnation region driven by the vortex spiral $m = +1$, $S = 1.02$, $Re = 1000$. (a–d) vertical slice of the jet; (e, f) horizontal slice at $x = 0.5D$. The distorted stagnation region is indicated by an arrow. The mode $m = +2$ has a moderately large amplitude, as shown in (b–f).

cases, $m = +1$ was the most unstable mode and grew dramatically downstream of the stagnation region, e.g. in figure 4(d) at $S = 0.9$ for a horizontal slice at $x = D$. Mode $m = +2$ was relatively strong upstream of the stagnation region (figure 4c) even when the flow was dominated by $m = +1$ downstream. Weak helical waves can also be observed together with the strong vortex spiral $m = +1$ in figure 4(d).

3.3.3. *Observation of weak helical waves with higher azimuthal wavenumber*

Along with the large-scale well-defined vortex spirals, there existed weaker and smaller-scale helical vortices, $m = +4$, $+5$ in figure 4(d). They do not appear in the vorticity contour pictures of figure 6, for example, where only those contours with high vorticity values are shown.

Further observation of these weak vortices was undertaken. By slowly traversing the horizontal laser sheet from the nozzle exit to downstream, these weak vortices were found to be composed of helical waves, which had similar temporal and spatial evolution to the strong helical waves. However these waves were much weaker, lacked organization and maintained their structure only for a short axial distance.

3.3.4. *Wave induced oscillation of the stagnation region*

As discussed in more detail in § 5 at large values of S, the mode $m = +1$ grew rapidly from the conical shear layer that made up the vortex breakdown. As a result there was an interesting interaction between it and the stagnation region. It distorted this region as it evolved and rotated around the axis. The result is shown clearly in figure 7 where the distorted tip of the stagnation region is shown to move in response to the wave rotation. In figure 7(a, b), the marked tip is shown interacting with the helical wave, marked vortex 1, as the wave moves around the stagnation region. The helical wave reappears as the marked vortex 2 on the left side in figure 7(c, d), and the marked, distorted tip moves with it. Similar migration of the distorted stagnation region is shown in figure 7(e, f) on a horizontal slice $x = 0.5D$. For this case, mode $m = +2$ still had a moderately large amplitude.

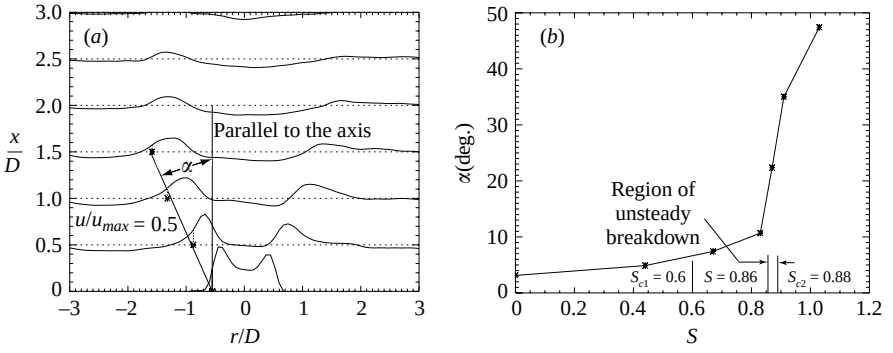

FIGURE 8. Spreading of jet with S increasing at $Re = 967$ for flow A. (a) Description of the half-angle α between the axis and the line of $u/u_{max} = 0.5$ on the axial velocity profiles for $S = 0.91$; (b) half-spreading angle of jets, α, versus S.

4. Quantitative flow measurements

4.1. *Preliminary measurements*

Measurements of the mean flow were made on flow A at $Re = 967$ with S varying from 0 to 1.1. In this section, time-averaged flow fields of the swirling jet are shown on a vertical cross-section which contains the axis and covers the region $x = 0$–$4.5D$, and on horizontal cross-sections at different axial locations, $x = 0$, $0.5D$, D, $1.5D$, $2D$, $3D$.

4.1.1. *Spreading of the mean flow*

Figure 8 demonstrates the spreading of the jet as S increased at fixed $Re = 967$, where the half-angle of spreading, α, is defined as the angle between the line joining the half-maximum axial velocity, $u/u_m = 0.5$ (that in the outer shear layer after vortex breakdown), and the line parallel to the axis. The behaviour of the spreading rate for large swirl number is different from that found by Chigier & Chervinsky (1967), for example, who found a smoothly increasing value of the half-angle as the swirl rate increased. As shown in figure 8 there was a much faster increase of the spreading rate as S approached and passed the critical value for vortex breakdown. At $S = 0.83$, the spreading rate becomes large far downstream, $x \leqslant 4D$, where a stagnation region formed. α reached 48° at $S = 1.03$ with the bubble located close to the nozzle exit.

4.1.2. *Centrifugal instabilities*

Compared with the non-swirling jet, the additional presence of swirl can result in an unstable radial stratification of the angular momentum, which leads to centrifugal instability. Rayleigh's inviscid criterion is a necessary and sufficient condition for instability for inviscid rotating flow:

$$\mathrm{d}\Gamma^2/\mathrm{d}r < 0,$$

i.e. the 'stratification' of angular momentum in a rotating flow is unstable if it decreases radially outwards. In the present experiments with the test tank stationary and $\Gamma > 0$ everywhere the inviscid criterion becomes

$$\mathrm{d}\Gamma/\mathrm{d}r < 0,$$

i.e. the azimuthal shear layer is centrifugally unstable if the circulation decreases in the radial direction from the rotating jet to the ambient fluid.

The theoretical profile of the dimensionless circulation in the jet in solid-body rotation is parabolic as a function of radius, at $x = 0$, and has a sharp peak at $r = R$ with a value of unity. After the peak, the circulation drops immediately to zero. However, in practice, this result could not be realized for several reasons. The laser sheet could only be placed close to the nozzle exit, i.e. $x = 3$–5 mm, not right at it, in order to have enough particles to define the flow, and, more importantly, to exclude the intense reflection from the nozzle which degraded the image. At this distance from the nozzle exit, no matter how short, the axial and azimuthal components of velocity had already diffused. Other technical limitations included: (i) The variable distance between the horizontal laser sheet and the CCD camera underneath the test tank. Thus our ability to zoom in was limited by the need to cover a large fraction of the flow field. (ii) The finite number of pixels of the CCD array used to capture the flow field. Thus in reality, the measured profiles close to the nozzle were smooth and continuous and had a peak lower than unity.

Figure 9 shows the spatial distribution of the time mean circulation and the corresponding axial vorticity,

$$\omega_x = \frac{1}{r}\frac{\partial wr}{\partial r},$$

at five axial stations, $x = 0, 0.5D, D, 1.5D, 2D$ for $S = 0.38, 0.78, 0.91, 0.98$ at $Re = 967$. For weakly swirling jets, say at $S = 0.38$, circulation profiles at axial locations relatively close to the nozzle, $x = 0$–$1.5D$, were similar and 'hill' shaped with the peak located at $r = 0.92R$. Downstream, $x \geqslant 2D$, the circulation distribution became flat with a relatively low amplitude due to the spreading and decay of the jet. The flow maintained solid-body rotation at small radii, and at large radii the circulation decreased and eventually dropped to zero. The jet flow could then be separated into two regions: the region before the maximum circulation is designated as the *vortex core*, and the area at larger radii as the *shear layer*. At steady state, fluid of the test tank was forced by vorticity recirculation to slowly co-rotate with the jet but with a much smaller angular momentum. The decrease in circulation in the azimuthal shear layer resulted in centrifugal instability/negative axial vorticity in all cases. The instabilities enhanced the mixing efficiency of the jet with the ambient fluid, and the flow decayed faster than a non-swirling jet. The solid-body rotating region, i.e. vortex core, was relatively stable or less turbulent since it was centrifugal stable.

When the swirl number increased further to $S = 0.78$, the circulation distribution at $x = 0$ was similar to that for $S = 0.38$, with almost the same value of the peak and reached this peak at the same radial location. Away from the nozzle exit, the maximum of the circulation amplitude decayed faster for larger swirl number and the region of decreased circulation spread out rapidly.

After vortex breakdown, $S > S_{c2}$, the circulation distribution was still 'hill' like at $x = 0$, reaching its maximum at the same radial location as for swirling jets before breakdown. But the amplitude of the maximum was slightly lower. Away from the nozzle exit, the circulation not only decayed faster, but its maximum was located at a larger radial position. This displacement of the circulation maximum to a larger radius, as well as that of the axial velocity maximum, is the signature of a vortex breakdown. The stagnation region was located around $x = 0.5D$ for these two swirl numbers. At $x = D$, downstream of the stagnation region, the maximum circulation was located further away from the axis, and even outside the region of investigation, e.g. at $S = 0.98$. In many ways it appeared as if the jet was split by an object inserted

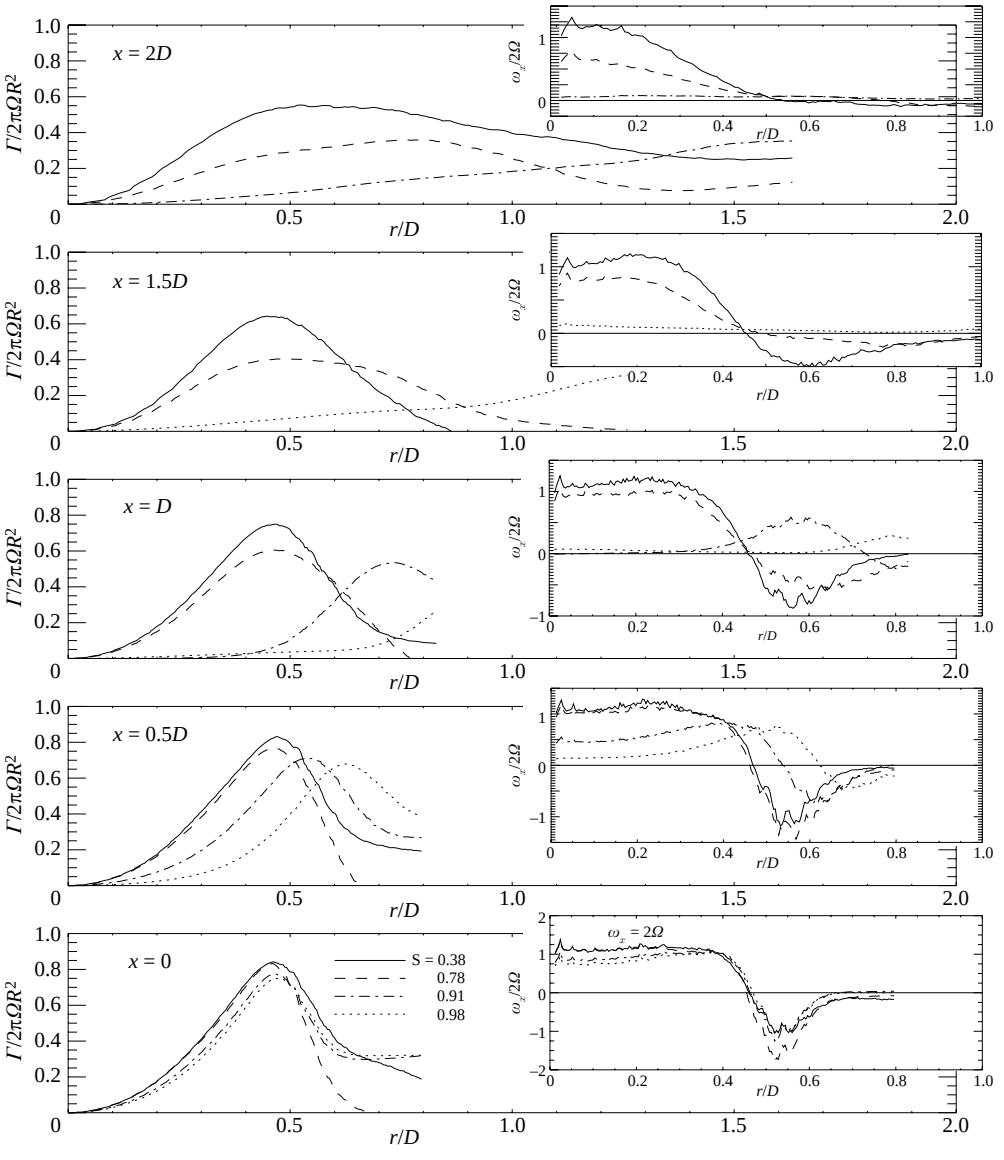

FIGURE 9. Dimensionless mean circulation and the corresponding axial vorticity versus r/D, for $S = 0.38, 0.78, 0.91, 0.98$, at axial locations $x = 0, 0.5D, D, 1.5D, 2D$, $Re = 967$ for flow A. ($N = 120$, $\Delta t = 0.4$ s).

into the flow. Within the breakdown structure, the circulation amplitude was almost zero.

4.1.3. *Criteria for breakdown from the measured velocity profiles*

Based on experimental, theoretical and numerical studies, Spall, Gatski & Grosh (1987) proposed a criterion for the onset of symmetric vortex breakdown that the Rossby number Ro (or inverse swirl ratio) satisfies:

$$Ro = u(r^*, x_0)/(r^*\Omega) \leqslant Ro_c = 0.65 \tag{4.1}$$

for $Re \geqslant 100$, where u is the axial velocity, r^* the radius of the maximum of the swirl velocity w, x_0 an axial location far upstream from the stagnation point, and Ω the core rotation rate near the vortex centreline $r = 0$. Based on previous theories and experiments, Billant *et al.* (1998) provided another criterion:

$$Si = \frac{\left[\int_0^\infty w^2(r, x_0)/r\,\mathrm{d}r\right]^{1/2}}{u(0, x_0)} \geqslant Si_c = 0.707, \tag{4.2}$$

and found a good agreement with their experiments for different Reynolds numbers and two nozzle diameters, $D_1 = 4$ cm and $D_2 = 2.5$ cm. Their critical Rossby number was calculated to be $Ro_c = 0.51$–0.65 for D_1 and $Ro_c = 0.80$–0.84 for D_2.

For the present experimental data, the criteria (4.1) and (4.2) were calculated close to the nozzle exit, $x_0 = 3$–5 mm, to give $Ro_c = 0.69$, $Si = 0.66$ for $S = 0.86$ and $Ro = 0.82$, $Si_c = 0.69$ at $S_{c2} = 0.88$. The critical swirl parameter of the present investigation, $Si_c = 0.69$ at $S_c = 0.88$, agrees with the value 0.707 proposed by Billant *et al.* (1998). The value of Si increased quickly for larger swirl rates as the bubble moved closer to the nozzle exit and caused $u(0, x_0)$ to decrease rapidly. The criterion based on the Rossby number only worked for the smaller swirl rate, at which condition, a symmetric yet unstable breakdown occasionally occurred downstream. $Ro_c = 0.69$ for $S = 0.86$ is quite close to the value 0.65 proposed for the onset of symmetric breakdown.

4.2. *Mean and fluctuating flow measurements*

The following measurements of the mean and the fluctuating flow and further instability analyses in § 5 are based on flow B.

Distributions of mean and root-mean-square (RMS) fluctuations of the axial and the radial velocity fields are shown in figures 10 and 11 for $S = 0$, 0.42, 0.71, 1.05, with the mean value, $\overline{u}$ or $\overline{v}$, in the left column and the RMS fluctuation, u' or v', in the right column. The Reynolds number was 1000. The amplitude of the mean velocities has been multiplied by 0.25 so that profiles with $0.25D$ axial distance between them do not overlap. The observation domain was chosen to focus on the region $0 \leqslant x \leqslant 2.5D$, where the most important instabilities were initiated and evolved.

4.2.1. *Mean components*

A weak initial over-shoot of the mean axial velocity at the jet edge found in flow A was eliminated in flow B, for which the turbulence level for the axial and the radial velocities was smaller at the spatial origin, and turbulence evolved slower with the fully turbulent region located further downstream. The jet characteristics were changed slightly by the change in the mean profiles, so that now the critical swirl number for stable vortex breakdown increased slightly from $S_{c2} = 0.88$ to $S_{c2} = 0.95$, indicated the sensitivity of this measurement to the details of the profiles and the difficulty in comparing exactly with previous results.

Before vortex breakdown, the form of the axial velocity profile was a flat-topped and became more jet-like downstream (figure 10). For strong swirl rates $S \geqslant S_{c2}$, vortex breakdown appeared on the jet axis. Around and downstream of the stagnation region, the axial velocity maximum was displaced radially from the axis, and the basic profile became wake-like. A reverse region with negative axial velocity was found downstream of the stagnation point. The breakdown structure moved upstream as S increased. At large swirl number, the stagnation point was located close to the nozzle exit, and then

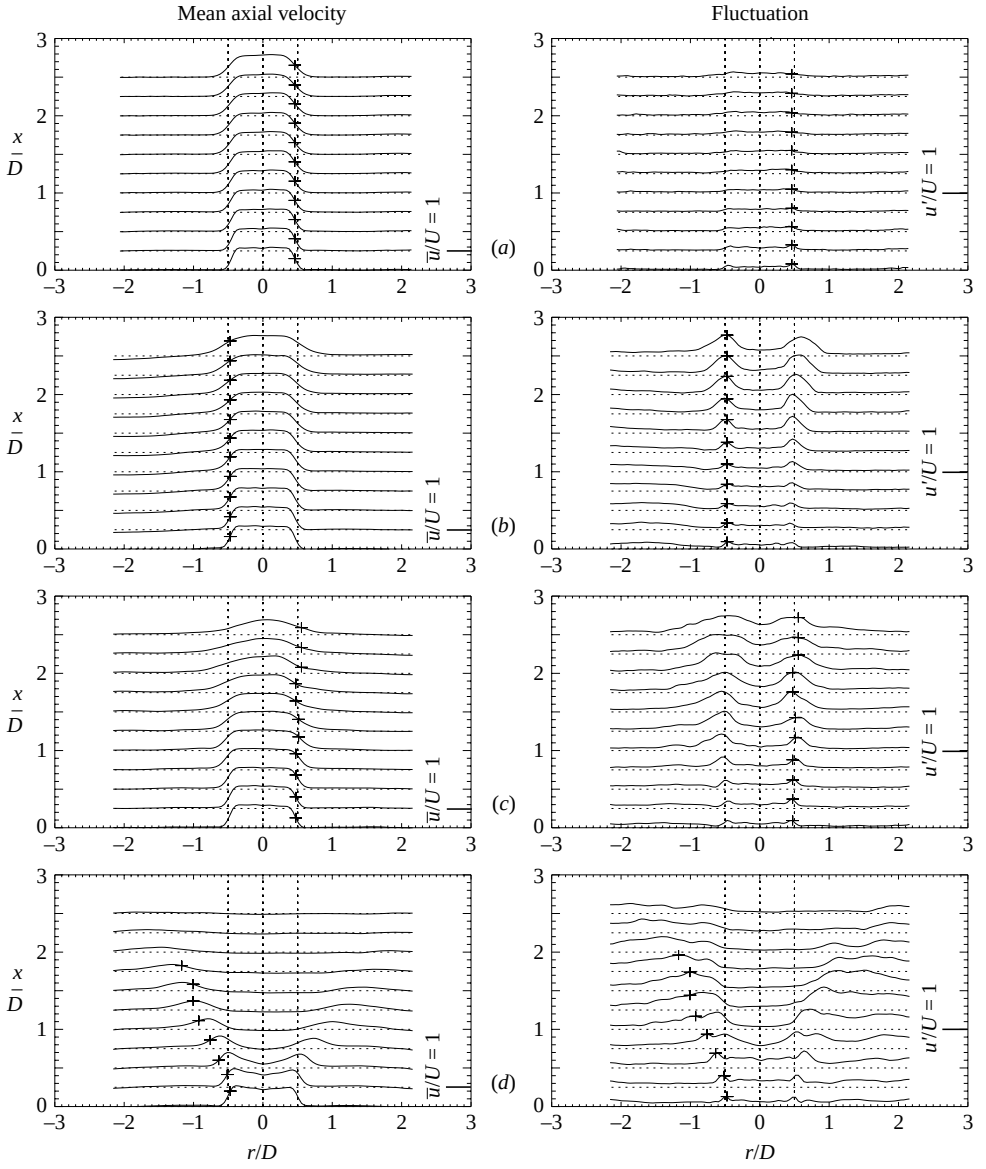

FIGURE 10. Left column: dimensionless mean axial velocity $\overline{u}/U$ ($\times 0.25$) versus r/D, right column: dimensionless RMS axial velocity fluctuation profiles u'/U versus r/D along the axis, at (*a*) $S=0$, (*b*) $S=0.42$, (*c*) $S=0.71$, (*d*) $S=1.05$, $Re=1000$, $N=120$, $\Delta t=0.4$ s. Flow B. Symbols + mark radial locations where further instability analysis was undertaken, see details in § 5.1.

the axial velocity at $x=0$ was of the wake type, i.e. the influence of the breakdown had propagated into the nozzle.

For all rotation rates up to breakdown, the radial velocity was up to 10% of U within the shear layer (figure 11). Only when the swirl rate was high enough for breakdown to occur, i.e. $S \geqslant S_{c2}$, was the mean radial velocity comparable with the other two components of velocity. This region of large mean value was located upstream and within the spreading jet between inner and outer shear layers.

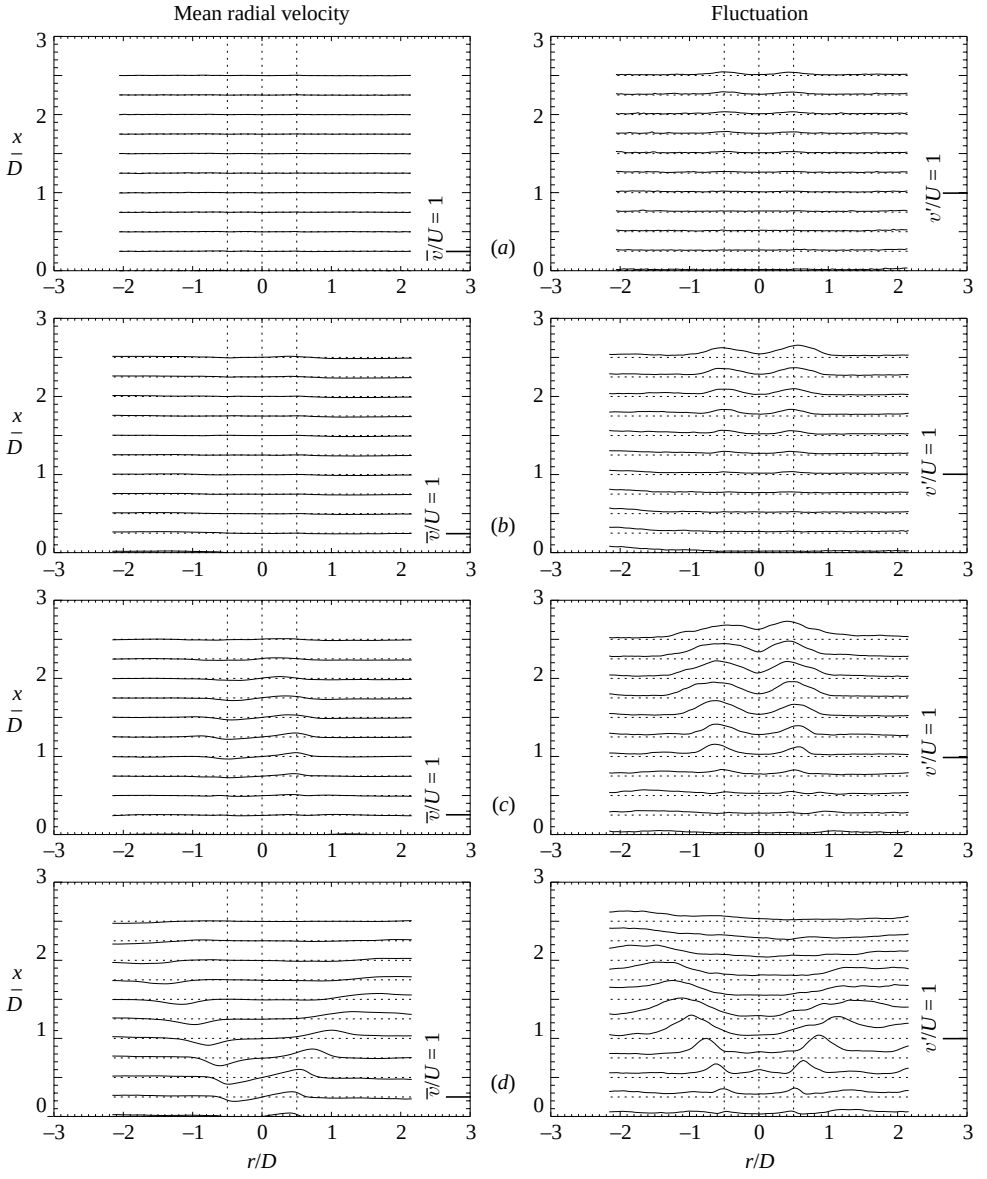

FIGURE 11. Left column: dimensionless mean radial velocity $\overline{v}/U$ ($\times 0.25$) versus r/D, right column: dimensionless RMS radial velocity fluctuation profiles v'/U versus r/D along the axis, at (*a*) $S = 0$, (*b*) $S = 0.42$, (*c*) $S = 0.71$, (*d*) $S = 1.05$, $Re = 1000$. ($N = 120$, $\Delta t = 0.4$ s). Flow B.

4.2.2. *RMS fluctuations*

For all flows, upstream of the fully turbulent region, the fluctuation distributions of the axial velocity had maxima off the axis with high levels of turbulence in the shear layer (both outer and inner shear layers after breakdown), and a low level of turbulence in the neighbourhood of the axis, i.e. in the vortex core and the bubble. The amplitude of turbulence increased and the high-turbulence region spread as S increased. Before vortex breakdown, fluctuation distributions far downstream, e.g. $x > 4D$ for non-swirling and weakly swirling jets and $x \geqslant 2.5D$ for strongly swirling jets, were

flat with high amplitude, while the turbulence level in the vortex core was comparable with that in the shear layer. The flow became fully turbulent in this region. The rapid mixing of the fluid in the shear layer and the vortex core was only observed in strongly swirling jets, while the non-swirling or weakly swirling jet reached its fully turbulent region further downstream and outside the observation frame. This fully turbulent region moved upstream and spread outwards and inwards as the swirl number increased. After vortex breakdown, $S > S_{c2}$, the downstream region of the jet, for example $x > 2D$ for $S = 1.05$, contained weak turbulent and mean flow. Turbulence in the wide reverse flow was relatively weak.

Before vortex breakdown, even though the mean radial velocity was weak when compared with axial and azimuthal components, relatively high levels of the fluctuating radial velocity appeared in the shear layer and the fully turbulent region, which shows that turbulence was always three-dimensional. After breakdown, for example at $S = 1.05$, the turbulent level in the radial velocity was high in the outer centrifugally unstable shear layer as shown in figure 11(d). The axial velocity fluctuation was large both in the inner and the outer shear layers, and the amplitude in the inner shear layer was found to be larger in figure 10(d).

4.2.3. *Spatial distribution*

The enhanced axial decay of the flow with increasing S, as demonstrated by the axial distributions of the maximum axial velocity (figure 12a) and the value on the centre-line (figure 12e), is consistent with the enhanced mixing and spreading of the flow by the introduction of swirl, especially after vortex breakdown. The amplitude of the mean radial velocity increased in the shear layer for strongly swirling jets, e.g. at $S = 0.71$ as shown in figures 11(c) and 12(c). Only when the swirl rate was high enough for breakdown to occur, i.e. $S \geqslant S_{c2}$, was the mean radial velocity comparable with the other two components of velocity, e.g. at $S = 1.05$ in figures 11(d) and 12(c).

The fluctuation of the axial velocity was relatively high at the spatial origin for the non-swirling jet, i.e. $u'_{max} = 0.08U$ at $x = 0$ for $S = 0$ (figure 12b). This turbulence was introduced by the facility. As mentioned earlier, we did not use a contraction at the nozzle exit, which would have produced a more laminar and uniform jet, but which would induce a jet-like inflow when the rotation rate was high (see e.g. Billant *et al.* 1998). This relatively high level of turbulence in the inflow decreased spatially within the laminar region, i.e. u'_{max} decreased to $0.05U$ at $x = 0.75D$. After that, u'_{max} started to increase axially but with a small amplitude, and reached $0.07U$ at $x = 2.5D$. For swirling jets, turbulence grew quickly in the shear layer, u'_{max} increased to $0.25U$ at $x = 1.75D$ for $S = 0.42$, and at $x = 1.25D$ with $S = 0.71$. After breakdown, u'_{max} was relatively high at the nozzle exit, e.g. $u'_{max} = 0.13U$ at $x = 0$ for $S = 1.05$. This maximum quickly increased to $0.3U$ at $x = 1.25D$, and decreased thereafter.

The spatial distribution of the maximum radial velocity fluctuation shown in figure 12(d) is similar to that of the maximum axial velocity fluctuation (figure 12b) except for the case with $S = 0.42$. Under this condition the radial velocity in the mean flow is hardly visible, and the radial velocity fluctuations are low upstream of the fully turbulent region.

Because of the technical difficulty of recording three components of the velocity, only two components were counted when calculating the turbulent kinetic energy of figure 12(f), the axial and radial velocity. We assumed that the spatial evolution of the turbulent kinetic energy in the azimuthal direction was similar to that in the axial and the radial directions, and the lack of the azimuthal component would have only a minor effect on our conclusions. Profiles of the integrated fluctuation of the kinetic

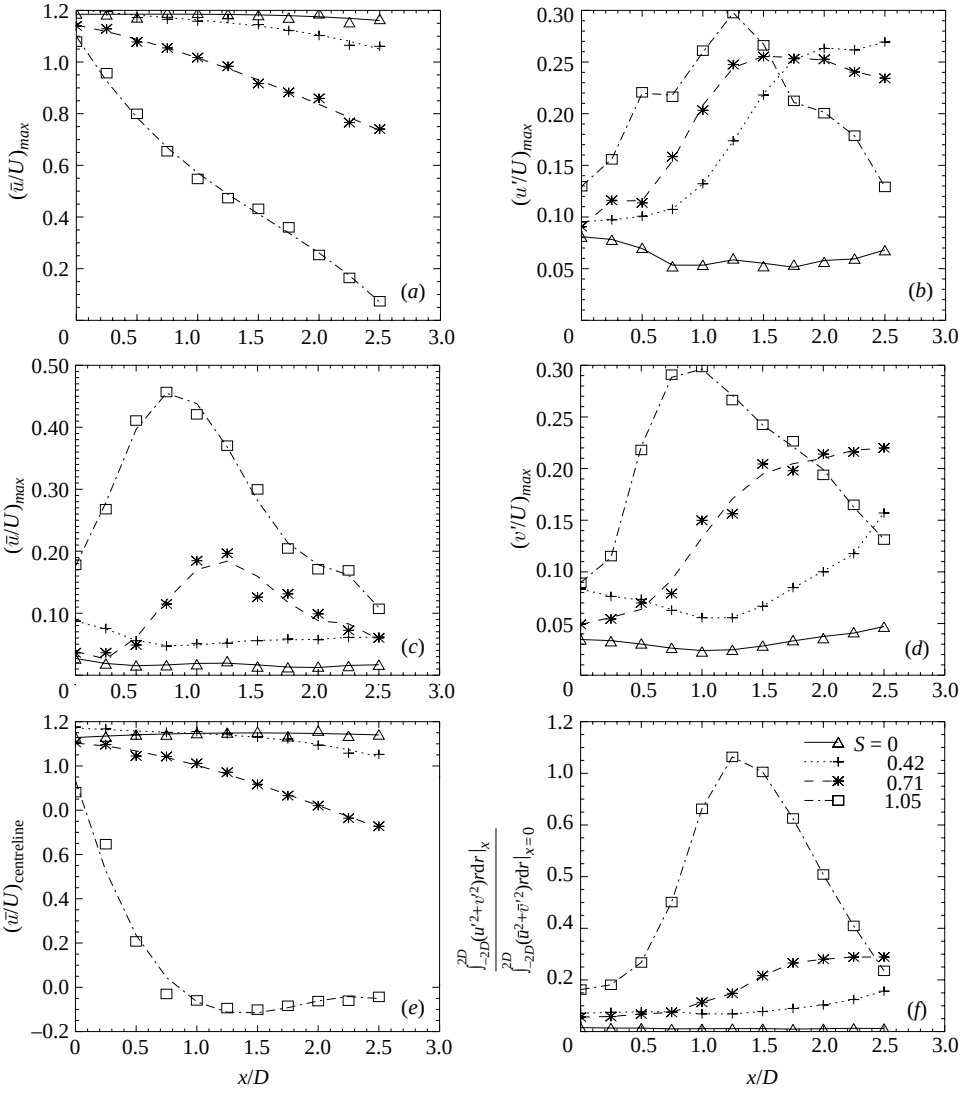

FIGURE 12. The spatial distribution of the maximum of (*a*) the mean axial velocity, (*b*) the RMS fluctuating axial velocity, (*c*) the mean radial velocity, (*d*) the RMS fluctuating radial velocity; (*e*) the mean axial velocity along the centreline; (*f*) the turbulent kinetic energy, at $S = 0,\ 0.42,\ 0.71,\ 1.05$, $Re = 1000$.

energy within the observation domain

$$x = [0, 2.5D],\ \ r = [-2D, 2D]$$

are plotted in figure 12(*f*) for $S = 0,\ 0.42,\ 0.71,\ 1.05$. This integrated value has been normalized by the kinetic energy in the mean flow at $x = 0$, i.e.

$$\frac{\displaystyle\int_{-2D}^{2D} (u'^2 + v'^2) r \,\mathrm{d}r|_x}{\displaystyle\int_{-2D}^{2D} (\overline{u}^2 + \overline{v}^2) r \,\mathrm{d}r|_{x=0}}.$$

For non-swirling jets, $S=0$, the perturbation level was low in the whole observational domain. As soon as rotation was introduced into the flow, the turbulent kinetic energy became larger at the nozzle exit. The profile was flat within the laminar region. After that, the amplitude started to grow and grew more quickly for the larger swirl numbers. After vortex breakdown, the turbulent kinetic energy was large at the nozzle exit and grew rapidly. The amplitude reached a large value downstream of the stagnation region and then decreased rapidly.

5. Self-excited oscillations

5.1. *Power spectra*

The spectra are represented by the power spectral density squared, psd^2, of the dimensionless axial velocity fluctuation:

$$psd = |\mathrm{FFT}[u'(t)/U]|, \tag{5.1}$$

where FFT is the fast Fourier transform, and $u'(t)$ is the fluctuation component of the axial velocity field, $u'(t)=u(t)-\overline{u}$, where $\overline{u}$ is the mean. In most cases, $u(t)$ was recorded for $N=120$ realizations with a sampling time step of $\Delta t=0.4$ s. After application of the FFT, the maximum resolvable frequency $f_{max}=0.5/\Delta t=1.25$ Hz, and the bandwidth or resolution $\Delta f=(1/\Delta t)/N\approx 0.02$ Hz. For the non-swirling jet, the axial shedding frequency of vortex rings was measured and presented as the dimensionless Strouhal number $Str=fD/U$ on a central, vertical slice of the flow. After the introduction of rotation, the azimuthal wavenumber, m, was used. It is defined as the frequency divided by the rotation rate (in revolution s^{-1}) of the nozzle exit, i.e. $m=f/\Omega$. This definition was deemed appropriate since it was observed that the wave rotated at the same rate as the basic rotation rate of the jet. For most cases, the high-amplitude peak at low frequencies/mode numbers which presents the underlying unsteadiness of the flow, has been filtered out to give better idea of the spectral distribution at interesting frequencies/mode numbers. The Reynolds number equals 1000 for all the power spectra presented below.

Power spectra were calculated at four swirl numbers $S=0,\ 0.42,\ 0.71,\ 1.05$, which represented the four regime discussed earlier: the non-swirling jet, weakly swirling jets, strongly swirling jets with vortex spirals $m=+2,\ +3$ before breakdown, and vortex breakdown with spirals $m=+1,\ +2$. To properly compare the spectral behaviour for different swirling rates, series of data were collected at radial locations where the RMS fluctuation amplitude reached its maximum in the shear layer (in the outer shear layer if the mean flow was wake-like), as marked by '+' in figure 10.

5.1.1. *Spectra are broadband at* $S=0$

For the non-swirling jet, at $S=0$, the spectra were broadband with low amplitude, $psd^2=0.00005$–0.0001, at all Strouhal numbers from the nozzle exit to $x\leqslant 2.5D$. The flow was laminar and no large-amplitude, vortex-ring-like structures were generated within the region of investigation.

5.1.2. *Spectra are locally peaked for* $S=0.42$

For the weakly swirling jet, e.g at $S=0.42$, the spectrum was still broadband at the nozzle exit $x=0$ but with the amplitude, $psd^2=0.0001$–0.0002, was higher than that at $x=0$ for the non-swirling jet. It was assumed that some turbulence had been introduced into the flow circuit at the rotating seal. At $x=0.25D$, the spectrum started to peak at $m=+2,\ +5,\ +6,\ +8$. Modes $m=+5,\ +6,\ +8$ decayed quickly and

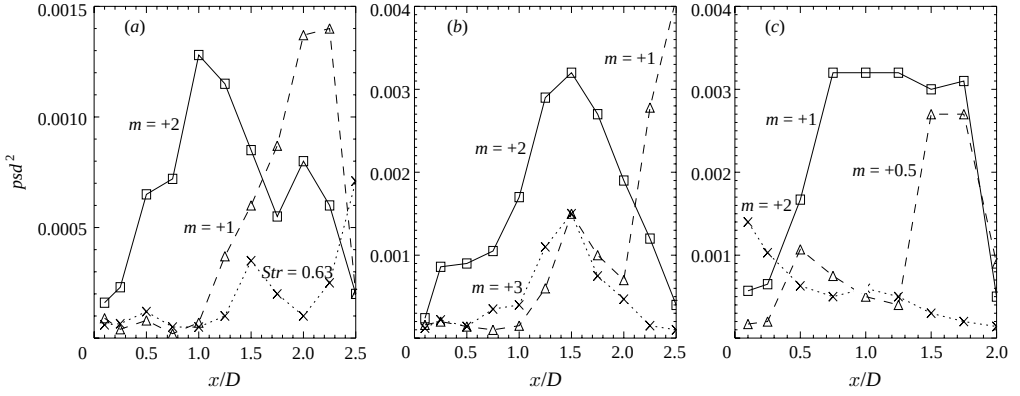

FIGURE 13. Spatial growth of spectra at $x = 0$–$2.5D$ for (a) $S = 0.42$, (b) 0.71 and (c) 1.05.

were ignored. Only the mode $m = +2$ grew in energy until $x = D$ and then decayed. At $x = D$, another mode, $m = +1$, appeared and started to grow. At $x = 2D$, mode $m = +1$ reached its maximum value in spectral energy, $psd^2 \approx 0.0013$, and then decayed quickly. Downstream, $x = 2.5D$, the spectrum became broadband but with an amplitude that was relatively high for $m \approx 4.5$ with corresponding Strouhal number $Str = 0.63$. This Strouhal number was close to the value for vortex rings generated downstream in non-swirling jets. In figure 13(a), the spatial growth and decay of the most unstable modes is evaluated from the peaks in the spectral distributions. Detailed spectral distributions at different swirl numbers can be found in Liang (2003).

5.1.3. *Spectral peak at* $m = +2$ *for* $S = 0.71$

For strong swirling jets before breakdown, e.g. at $S = 0.71$, the spectrum was broadband with $psd^2 = 0.0001$–0.0002 at the nozzle exit but with relatively high amplitude, $psd^2 = 0.0002$–0.00035, at $m = +2$ and $+4$. Away from the nozzle exit, $m = +2$ peaked quite obviously and grew quickly when propagating downstream. It reached its maximum $psd^2 \approx 0.0032$ at $x = D - 1.5D$ and then decayed. At $x = 2.25D$, mode $m = +1$ suddenly peaked with high amplitude and immediately grew to $psd^2 \approx 0.004$ at $x = 2.5D$. It was not clear if $m = +1$ was another unstable mode independent of mode $m = +2$, or is the subharmonic mode of $m = +2$ due to possible vortex pairing downstream. Mode $m = +3$ appeared in the shear layer in the interval $0.75D \leqslant x \leqslant 2D$, but with relatively low amplitude, $psd^2 \leqslant 0.0015$, which was of the same order as the locally unstable modes $m = +2$ and $+3$ observed at $S = 0.42$. Figure 13(b) shows the spatial evolution of the spectral peaks.

5.1.4. *Spectral peak at* $m = +1$ *for* $S = 1.05$

For strongly swirling jets after breakdown, e.g. at $S = 1.05$, the spectrum was no longer broadband at the nozzle exit $x = 0$, and $m = +2$ had a strong peak with amplitude $psd^2 \approx 0.0014$. Away from the nozzle exit, $m = +2$ decayed smoothly and continuously. Mode $m = +2$ still had a distinct peak at $x = 0.25D$ and then degenerated into background noise for $x \geqslant 0.5D$. As $m = +2$ lost its distinctness, mode $m = +1$ started to play a major role in the spectral distribution at $x \geqslant 0.5D$. Mode $m = +1$ appeared at the spatial origin $x = 0$ but with a relatively low amplitude $psd^2 = 0.0003$, and then it grew to $psd^2 = 0.0007$ at $x = 0.25D$. Thereafter it grew rapidly and reached saturation at $x = 0.75D$ with the spectra energy maximum

$psd^2 = 0.0033$. This strong mode maintained its high energy for a relatively larger axial distance, i.e. $x = 0.75D$–$1.75D$. Another strong mode $m = +0.5$ suddenly peaked at $x = 1.5D$ with spectra energy $psd^2 = 0.0027$ and remained with this high energy to $x = 1.75D$. At $x \geqslant 2D$, the peaks of both strong modes $m = +0.5$ and $m = +1$ disappeared, and the spectrum became broadband with high energy distributed at low frequencies. After breakdown, some nonlinear secondary interactions may occurred in the flow downstream, say $x \geqslant 2D$, and the widely spread jet became fully turbulent. The spatial evolution of the spectral peaks is shown in figure 13(*c*).

5.1.5. *Conclusion to* § 5.1

Vortex rings, $m = 0$, dominated non-swirling and weakly swirling jets but they were, at most, convectively unstable, and were excited by external noise and convected away by the mean flow. In both weakly and strongly swirling jets before breakdown, the helical wave $m = +2$ peaked, grew and then decayed when propagating with the mean flow. However, based on analytical observation and spectral study, it is suggested that for weakly swirling jets this helical wave was excited by some external perturbation, which might have been introduced from the rotating seal and evolved as moderately low-level noise at the nozzle exit. First, the spectral maximum it could reach in weakly swirling jets was significantly smaller, e.g. 2.5 times smaller at $S = 0.42$ than for strongly swirling jet at $S = 0.71$. Secondly, downstream, before the fully turbulent region, the spectra peaked at a Strouhal number close to the value for non-swirling jets, i.e. tilted vortex rings dominated the shear layer as shown in earlier observations (figure 3*b*). Lastly as discussed in § 3.1, helical waves grew stronger when a vortex ring passed by from upstream and became weak or even disappeared as the vortex ring propagated further downstream. The LadHyX group also observed and reported this phenomena.

To certify whether oscillations generated at $S = 0.71$ and 1.05 are the consequence of global instabilities, it is first necessary to rule out the possibility that these oscillations are caused by some discrete, strong, external forcing specific to our facilities. Recall the broadband power spectra distribution at the nozzle exit and at $x = 2.5D$, under conditions $S = 0$ and 0.42. They reveal an absence of discrete forcing frequencies at $m = +1$, $+2$ or their harmonics, either from the flow at the nozzle exit or from the fluid exiting the tank. This suggests that the background forcing is not the cause of the distinct spectra peaks at $S = 0.71$ and 1.05. These distinct peaks in the spectral records indicate the possible existence of limit-cycle modes. But this is only a preliminary conclusion, and further investigations need to be carefully designed and performed.

5.2. *Hopf bifurcation*

A second experiment was performed to establish whether the oscillations are an indication of the existence of a super-critical Hopf bifurcation, which can be modelled by the super-critical Landau equation.

As reviewed by Huerre & Monkewitz (1990), near critical conditions, the characteristic overall amplitude $|A|$ of the global response is governed by the forced Landau equation (Landau & Lifshitz 1959):

$$\mathrm{d}|A|/\mathrm{d}t = \alpha_1|A| - \alpha_2|A|^3 + \alpha. \tag{5.2}$$

The constant α_1 determines the temporal amplification rate during the period of exponential growth if the bifurcation is super-critical, i.e. when $\alpha_2 > 0$ and $S > S_k$. S_k is the critical control parameter, when the Reynolds number is fixed, at which the oscillation first emerges first and α is the external forcing. When there is no forcing

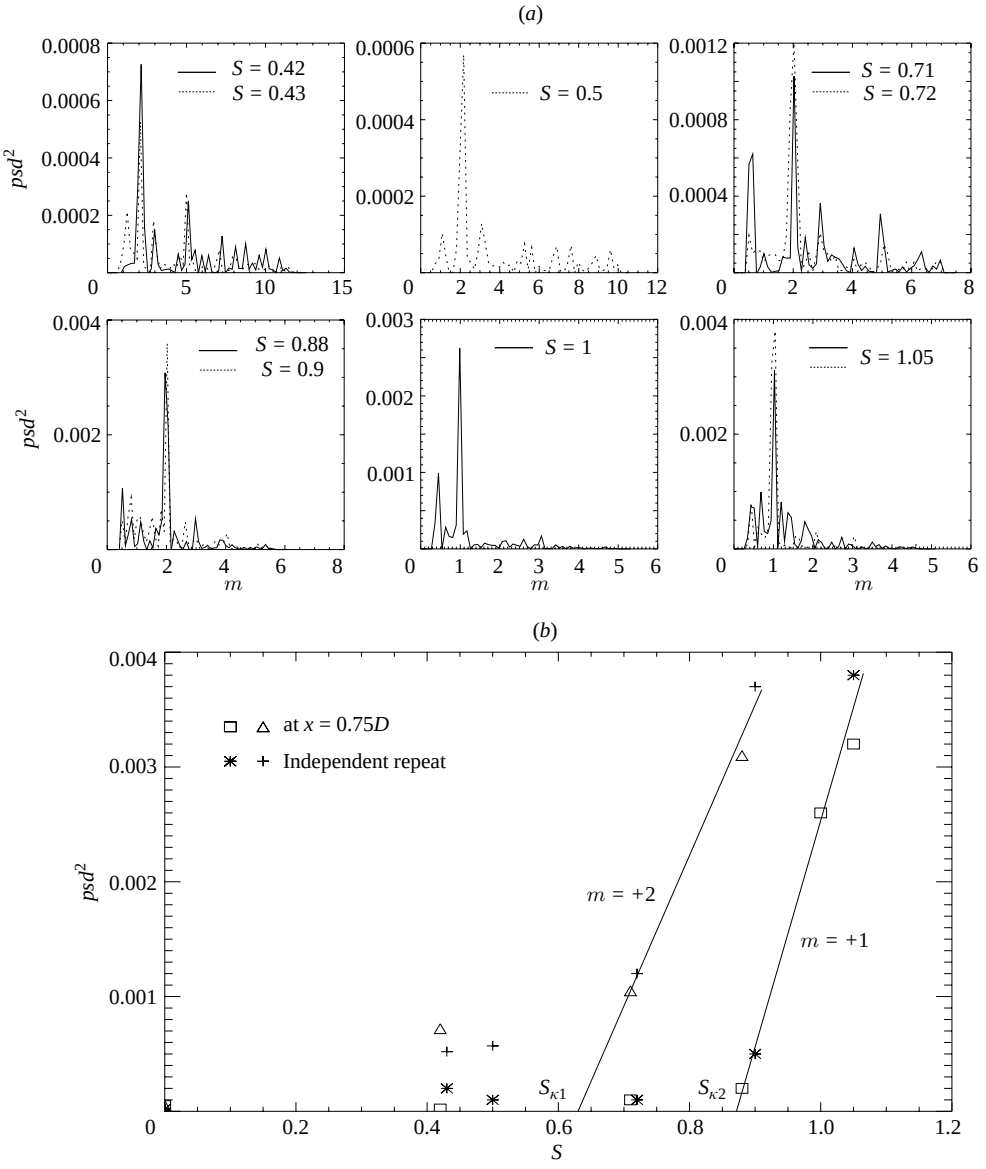

FIGURE 14. (*a*) Spectral distribution at $x = 0.75D$, for $S = 0.42$, 0.71, 0.88, 1, 1.05, shown by solid lines. Experiments were repeated independently at $S = 0.43$, 0.5, 0.72, 0.9, 1.05, shown by dashed lines. (*b*) The impulsive increase of the spectral energy versus swirl number S shows the appearance of Hopf bifurcations at S_{k1} and S_{k2} for modes $m = +1$ and $+2$.

of the flow, i.e. $\alpha = 0$, the saturation amplitude satisfies

$$|A|_{sat}(\alpha = 0) \approx \alpha_3 (S - S_k)^{1/2} \tag{5.3}$$

when $S \geqslant S_k$, where α_3 is a positive constant and can be expressed in terms of α_1 and α_2.

The spectral energy distribution at the axial location $x = 0.75D$ is shown by solid lines in figure 14(*a*), for $S = 0$, 0.42, 0.71, 0.88, 1, 1.05. The amplitude of the spectral energy of modes $m = +1$ and $+2$ is plotted in figure 14(*b*) by a square and a triangle

symbol respectively. Experiments were repeated independently at $S = 0$, 0.43, 0.5, 0.72, 0.9, 1.05, and corresponding results are plotted by dashed lines in figure 14(a) and star and plus symbols in figure 14(b).

The profile of the amplitude of spectral energy versus the swirl number reveals that the saturation amplitude of two modes, $m = 2$ at $S \geqslant S_{k1}$ and $m = +1$ at $S \geqslant S_{k2}$, can be modelled by the solution to the unforced super-critical Landau equation

$$psd^2 = |A|^2_{sat}(\alpha = 0) \propto (S - S_k). \tag{5.4}$$

The linear amplitude dependence was extrapolated to predict the critical swirl number when $|A|_{sat} = 0$. Two critical swirl numbers have been found, $S_{k1} = 0.62$ for $m = +2$, and $S_{k2} = 0.87$ for $m = +1$. S_{k1} is close to the critical value $S_{c1} = 0.6$ which separates the weakly and strongly swirling regimes for flow A. A non-zero forcing amplitude, which is never achievable in experiments, may lead to an under-prediction of critical values of the Hopf bifurcation from a plot of $|A|_{sat}$ versus $(S - S_k)^{1/2}$. Thus the real S_{k2} most likely coincides with the critical swirl number for vortex breakdown of flow B, $S_{c2} = 0.95$. Hereafter we will use S_{c1} and S_{c2} as the appropriate critical parameters.

It should be noted that unlike theoretical or numerical studies, the external forcing is always present in experiments. This non-zero forcing amplitude became larger as soon as rotation was introduced into the system and spatially increased as the vortex grew and propagated, e.g. $|A|^2_{sat}(\alpha = 0) = 0.00065$ for $m = +2$ and 0.00015 for $m = +1$ at $x = 0.75D$. To avoid this difficulty and thereby under-evaluate the critical swirl number when a Hopf bifurcation was initiated, a least-square-error fitting was carried out relying on points with relatively large spectral energy $|A|^2_{sat}(\alpha)$, i.e. at larger swirl numbers. For a rapidly increasing function, this fitting and the calculated criterion S_k should be more reliable than calculations which include the questionable points at smaller swirl numbers. However, it is understood that the existence of the moderately high external noise in weakly swirling jets and high turbulence level for strongly swirling jets makes the instability nature elusive for mode $m = +2$ before breakdown, and any discussion about it remains only as a suggestion and awaits further clarification.

The saturation amplitude of vortex spirals $m = +1$ and $+2$ has been found to be proportional to $(S - S_c)^{1/2}$. This linear dependence is strong circumstantial evidence that these two oscillations are of the super-critical Hopf bifurcation type.

5.3. *Forced experiments*

Experiments were performed to study the influence of external forcing on the strength of the oscillations in the flow shear layer and, thereby, determine whether the flow response was due to self-excitation or the continuous spatial amplification of disturbances from upstream. If the swirling jet was dominated by the spatially amplifying disturbance for $S < S_c$, we would expect that the shear-layer response to external excitation would be proportional to the forcing level. If, in fact, a global mode emerged for $S > S_c$, the flow would become dominated by an amplifying perturbation, which would eventually saturate and render the flow insensitive to low-level external forcing.

As reviewed by Huerre & Monkewitz (1990), the forced Landau equation (Landau & Lifshitz 1959) with low-amplitude forcing is of the form

$$|A|_{sat}(\alpha) = |A|_{sat}(\alpha = 0) + \frac{\alpha}{2[|A|_{sat}(\alpha = 0)]^2} \tag{5.5}$$

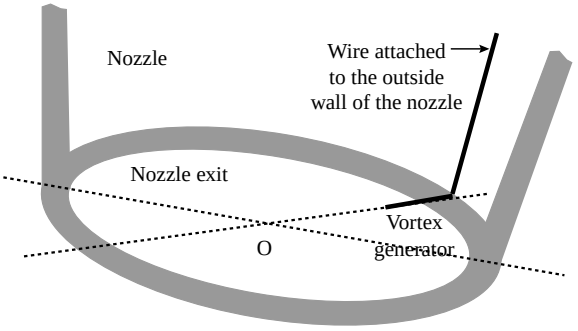

FIGURE 15. Forced experiments: vortex generators are attached to outside of the nozzle and inserted into the flow at the nozzle exit. Forcing of $|m| = 1$ mode is shown.

when $\alpha \ll [|A|_{sat}(\alpha = 0)]^3$. For a globally stable system which may be convectively unstable or locally absolutely unstable, the flow response is linearly dependent on low-level external forcing α. According to experimental observations, some spatially developing flows, e.g. co-flowing mixing layers, homogeneous jets, wakes at Reynolds numbers below the onset of the von Kármán vortex street, and boundary layers on a flat plate, behave as 'noise amplifiers'. Another class of spatial developing flows which are self-excited and sufficiently super-critical, are globally unstable and called 'flow oscillators'. This kind of oscillation has a well-defined frequency throughout the whole flow, and its amplitude is insensitive to external excitation, i.e. $|A|_{sat}(\alpha) = |A|_{sat}(\alpha = 0)$. Good examples are mixing layers or jets with a sufficiently large counter-flow (Strykowski & Niccun 1991), hot jets (Monkewitz *et al.* 1990), wakes at Reynolds numbers above the onset of the von Kármán vortex street (Mathis, Provansal & Boyer 1984; Strykowski 1986; Monkewitz 1988), and boundary layers on a rotating disk (Lingwood 1995, 1996).

External forcing at the observed strong helical mode numbers was provided by vortex generators mounted at the nozzle exit. Wires were attached to the outside wall of the nozzle, with the perpendicular end pointed to the centre of the nozzle exit at $x = 0$ (figure 15). The part inserted into the flow had three length scales, l_x, l_r and l_θ in the axial, radial and azimuthal direction respectively. Either one or two vortex generators were applied to introduce external forcing with helical wavenumber $m = +1$ or $+2$. The amplitude of forcing was specified by the azimuthal length inserted into the flow, l_θ, for which three values, 0.01, 0.05 and 0.15 in. were used. For all cases, $l_x = 0.025$ in. and $l_r = 0.075$ in. were fixed.

The profile of the amplitude of flow response (represented by the *psd* at $m = +1$ or $+2$) versus the forcing level (represented by l_θ/D) at each forcing mode for different swirling rate, is plotted in figure 16. The power spectral amplitude was still calculated at the radial location with the maximal RMS value in the shear layer (outer shear layer if the axial velocity was wake-like).

At the axial location $x = 0.75D$ when the flow was being forced at $m = +1$ (figure 16*a*), the flow response increased proportionally to the forcing level until the forcing level was relatively high for $S = 0$, 0.42, 0.71, while the flow response seemed insensitive to external forcing at $S = 1.05$. We believe that this insensitivity was caused by the temporal amplification and saturation of the global mode $m = +1$.

At the same axial location $x = 0.75D$ but when the flow was being forced at $m = +2$ (figure 16*b*), the flow response was insensitive to the forcing level for $S = 0.88$, which provided strong evidence that the global unstable mode $m = +2$ has emerged.

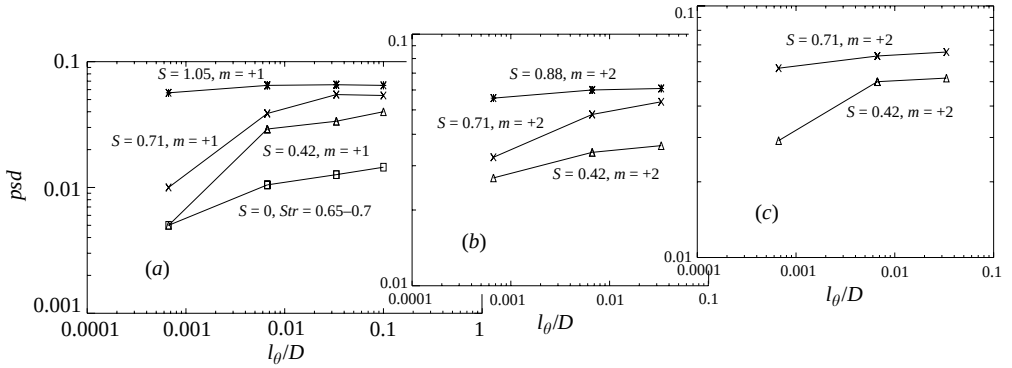

FIGURE 16. Response of the shear layer of swirling jets to forcing at $m = +1$ or $+2$. The forcing level is specified by the dimensionless azimuthal length of the vortex generator inserted into the flow, l_θ/D. The amplitude *psd* is the power spectra of the dimensionless axial velocity. (*a*) forcing at $m = +1$, data collected at $x = 0.75D$; (*b*) forcing at $m = +2$, data collected at $x = 0.75D$; (*c*) forcing at $m = +2$, data collected at $x = 1.5D$.

However, the spectral amplitude increased linearly with the forcing level at $S = 0.71$, and the forcing seemed not have much effect on the shear layer with $S = 0.42$. Under relatively more stable conditions, such as at $S = 0.42$ and 0.71, the spatial amplification of the external or self-excitation perhaps had not evolved enough at the axial location $x = 0.75D$, thus might not give an accurate conclusion. The axial location of the investigation was then increased to $x = 1.5D$ for $S = 0.42$ and 0.71 with the flow being forced at $m = +2$. Figure 16(*c*) shows the insensitivity of the shear layer to external forcing for $S = 0.71$, and linear dependence when $S = 0.42$. This suggests that the globally unstable mode $m = +2$ eventually emerged at the strong swirling rates before vortex breakdown.

Comparisons of instantaneous unforced and forced flow fields, e.g. vorticity contours, do not reveal any clearly significant differences. The results of figure 16 appear to be the most suitable way of determining any differences that do in fact exist.

It is understood that the evidence provided above does not furnish conclusive proof that the bifurcation observed at $S > S_c$ is the consequence of an unstable global mode. This conclusion can only be verified by including an investigation of the transient flow response.

5.4. *Transient experiments*

Due to the moderately high amplitude of mode $m = +2$ before S_{c1}, it is difficult to capture the transient growth of this mode by rapidly increasing the rotation rate from below the critical value to above.

Fortunately, the mode $m = +1$ evolved as, at most, a weak mode for $S < S_{c2}$ especially upstream, but grew quickly for $S > S_{c2}$ and reached its maximal amplitude while it was still close to the nozzle exit. From careful observations of the flow as a stagnating point/region formed downstream, moved upstream and stabilized at a certain axial location, an interesting phenomenon was noted. The vortex spiral $m = +1$ evolved quickly and became strong in the shear layer only after the bubble had moved upstream and found a stable location. The exponential growth of $m = +1$ may be recordable during the relatively long process of bubble generation and stabilization

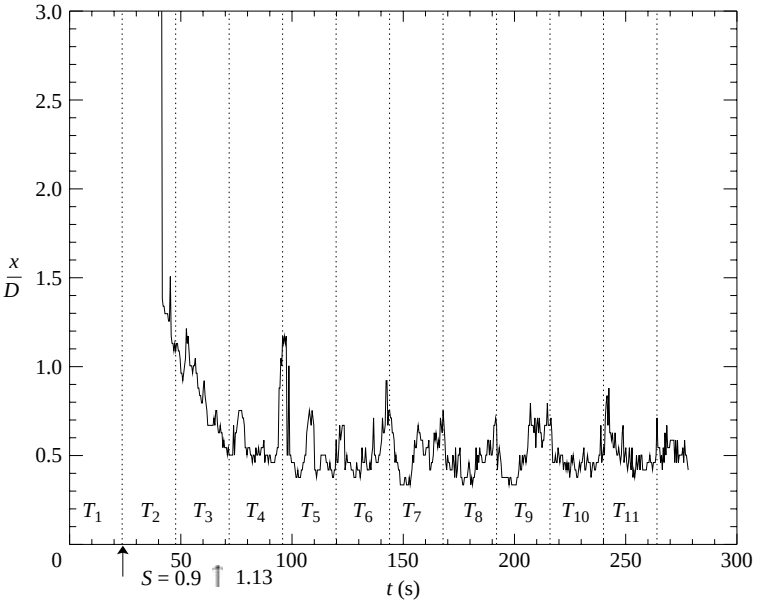

FIGURE 17. The axial location of the stagnation point versus time. Impulsive increasing of swirl number from $S = 0.9$ to 1.13 takes place at time $60\Delta t = 24$ s.

if we set the final swirl number close to S_{c2}. Thus, after increasing the swirl number impulsively from $S < S_{c2}$ to $S > S_{c2}$, the damping of mode $m = +2$ could be observed and then the appearance and amplification of $m = +1$ at the appropriate locations.

5.4.1. *Generation of the mode* $m = +1$

Limited by the present data capture and recording capacity, initial and final values of swirl number were chosen as $S = 0.90$ and 1.13 respectively. The footprint of the vortex breakdown was recorded by the time history of the axial location of the stagnation point along the centreline, as shown in figure 17. $N = 60$ instead of 120 was used to calculate the mean, RMS and spectra of velocity fields during each period of $\Delta T = N\Delta t = 24$ s, with $\Delta t = 0.4$ s. The history was divided into 11 time periods T_1 to T_{11}. Impulsive (in 0.5 s) increase of the swirl number from $S = 0.9$ to 1.13, was performed at time $t = 60\,\Delta t = 24$ s, at the beginning of the period T_2. The stagnation point first appeared around $x = 1.3D$ at $t = 43$ s and then moved upstream. It reached $x = 0.5D$–$0.6D$ at $t = 72$ s and stayed there, oscillating with low amplitude (figure 17).

To keep data spatially consistent before and after the breakdown occurred, the point for spectral study had to be chosen close to the nozzle exit where the flow had not yet spread much after vortex breakdown. At the same time, this point had to be far enough away from the nozzle exit to capture the evolving instabilities. The location, $x = 0.25D$ and $r = 0.45D$, was chosen and is marked as '+' in the mean axial velocity field (figure 18) during each period.

As shown in the spectra of figure 18(*b*) (i), mode $m = +2$ has a distinct peak with high amplitude, $psd^2 \approx 0.003$, during the period T_1 when $S = 0.90$. The spectra are low and flat at all other mode numbers. After the swirl number was increased impulsively to $S = 1.13$ at $t = 24$ s, the end of T_1, the mode $m = +2$ damped immediately and the spectral distribution became broadband during the transition T_2 to T_4 (figure 18*b* (ii–iv). Mode $m = +1$ started to peak during the period T_4 to T_5 (figure 18*b* (v)) and

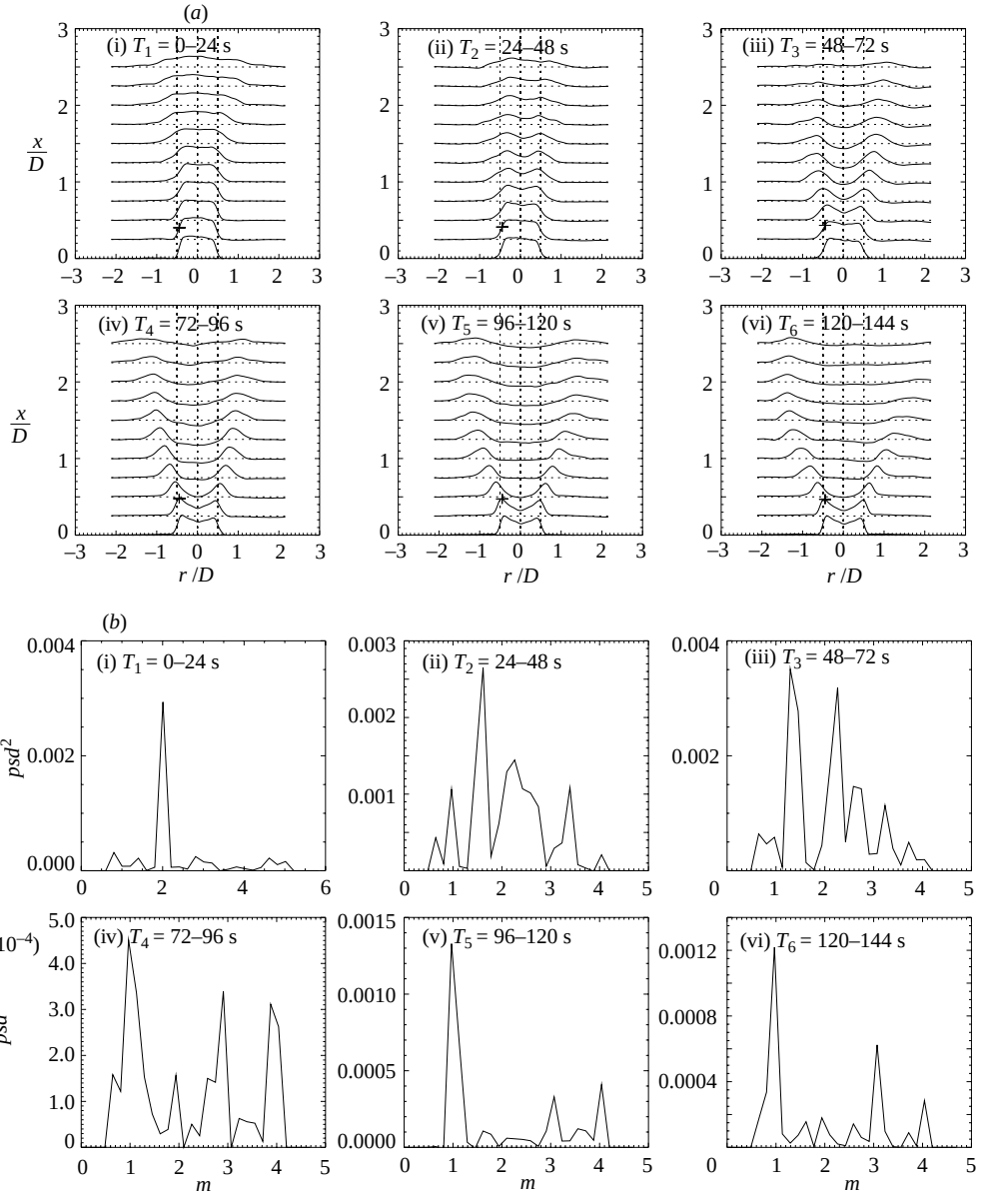

FIGURE 18. (*a*) The mean axial velocity field during each time period, and (*b*) the spectral distribution, psd^2, at the location marked by +, i.e. $x = 0.25D$, $r = 0.45D$.

maintained this distinctness thereafter. The amplitude of the spectral energy for mode $m = +1$ increased a little and eventually oscillated with magnitude $psd^2 = 0.0018$–0.0025.

The observation of the emerging and growth process of the mode $m = +1$ after the rapid increase in swirl number demonstrates that $m = +1$ results from the temporal amplification of the impulse response and finally this oscillation overwhelms the whole area. We conclude that the vortex spiral $m = +1$ is an unstable global mode for $S > S_{c2}$.

5.4.2. *Growth rate of the mode* $m=+1$ *at* $x=0.25D$, $r=0.45D$

Efforts were made to record the exponential growth of the mode $m=+1$ after breakdown had stabilized upstream, and calculate the growth rate α_1. For an unstable global/self-excited oscillation, $|A|$ is governed by

$$\mathrm{d}|A|/\mathrm{d}t = \alpha_1|A|, \implies \log_e|A| = \alpha_1 t + \text{constant}. \tag{5.6}$$

The turbulence level was already high before breakdown due to the existence of the strong mode $m=+2$ and a large amount of random turbulence. Thus we could not capture the temporal growth of $m=+1$ by simply tracing the RMS amplitude of fluctuating velocity fields in the shear layer. We had to measure the growth of $m=+1$ using a spectral study.

Based on the same data series, but using $N=20$ to distinguish the integer mode number in the spectral distribution, the amplitude of spectral energy at $m=+1$ is calculated as $psd^2=0.0002$ at $t=72$–80 s, 0.0007 at $t=80$–88 s, and 0.0019 at $t=88$–96 s (detailed distributions can be found in Liang 2003). The exponential growth rate of the mode $m=+1$ at $S=1.13$ was estimated to be $\alpha_1=0.071$ by a first-order polynomial fitting, i.e. $\ln(psd)=0.071t+\text{constant}$. It is close to the value calculated by Ruith *et al.* (2003) for the unstable global mode $m=+1$ in their case at $S=1.095$, $\alpha_1=0.066$.

5.4.3. *Spatio-temporal growth of mode* $m=+1$

The answers to some questions still remained elusive, such as: When and where was the instability initiated, i.e. where was the wave maker? Downstream, in the wake region, in the inner shear layer of the breakdown structure which was centrifugally stable, or in the outer shear layer which was centrifugally unstable? When and how did these instabilities amplify, expand, overwhelm the whole flow and become globally unstable/self excited? Thus not only must the temporal growth of the instability wave $m=+1$ at one position be measured, but also the whole flow needed to be studied further.

From careful study of the spectral distribution at each radial and axial location during every period, which is now 8 s long for $N=20$ and $\Delta t=0.4$ s, the spatio-temporal growth of the instability wave $m=+1$ was revealed and is shown in figure 19. Here, the study is limited to the region $r=[-2D, 0]$ and $x=[0, 1.25D]$.

The first and probably the most interesting observation is that the wave $m=+1$ first appeared in the vortex core during the period $t=32$–40 s in figure 19(*e*), before a clear indication of the stagnation due to vortex breakdown could be observed in the mean axial velocity distribution in figure 19(*f*) $t=40$–48 s. After checking instantaneous vector images during those two periods, i.e. $t=32$–40 s and $t=40$–48 s, the earliest time for the formation of the stagnation point/region was found to be $t=41.6$ s. A wake region did exist along the axis during the period of figure 19(*e*), $t=32$–40 s, with a structure like a tadpole with the head reaching upstream to $x=D$ and a following tail at $x\geqslant 1.5D$ (see figure 20*a* at $t=38.3$ s). A wave packet of $m=+1$, $x=[D, 1.25D]$ and $r=[0, 0.008D]$, first appeared within the head of the tadpole shape (figure 19*e* at $t=32-40$ s).

At $t=41.6$ s, the stagnation point/region formed within the wake structure and vortex breakdown occurred. This breakdown structure had three stagnation points with two 'one-cell' bubbles in between, one centred at $x=1.4D$ and the other centred at $x=1.8D$ (figure 20*b* at $t=44.4$ s). The existence of the helical wave $m=+1$ in the vortex core (figure 19*f* at $t=40$–48 s) might be responsible for the deficit of bubbles on the right side of the axis. These two one-cell bubbles were very unsteady and

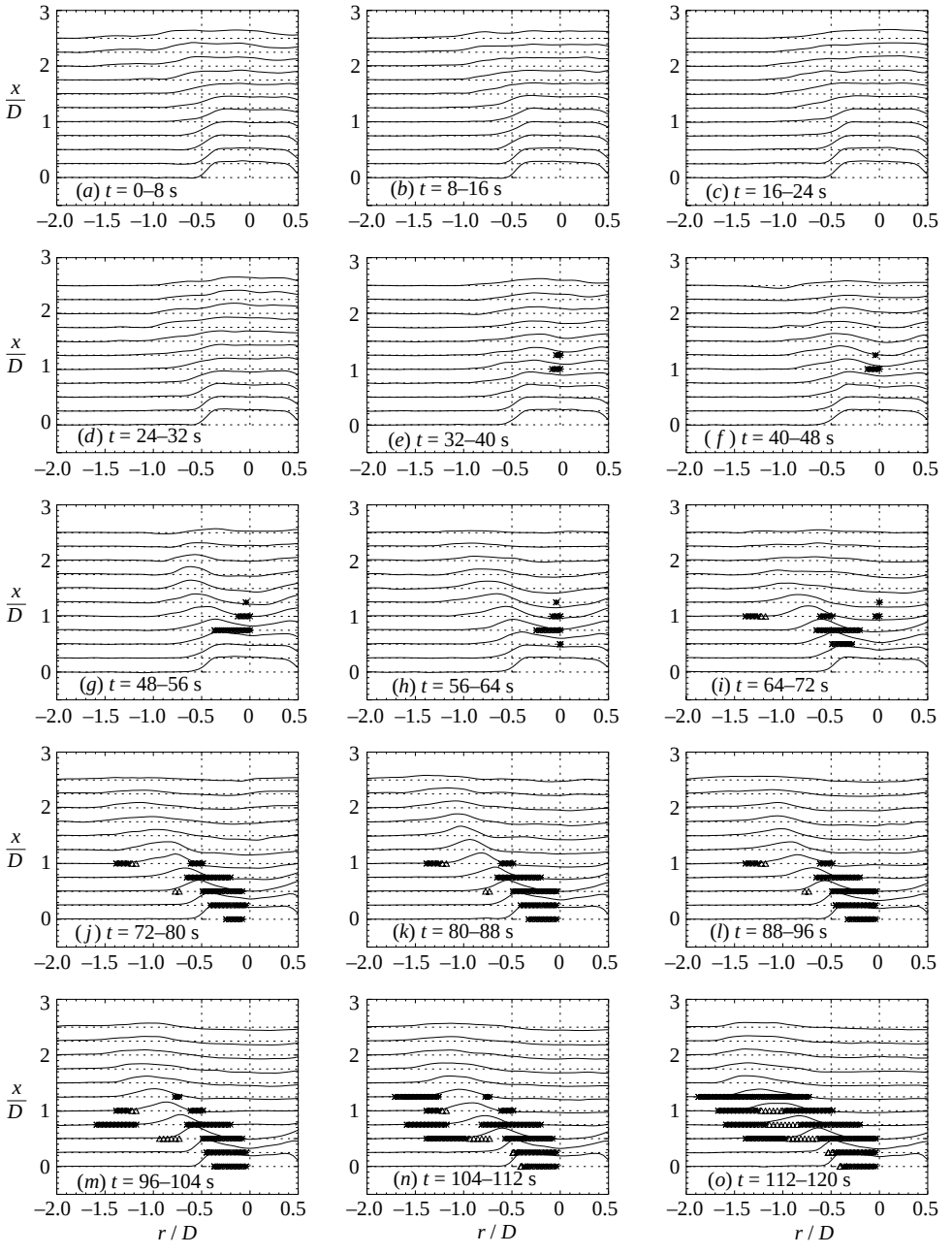

FIGURE 19. The location of spatio-temporal growth of wave $m = +1$ is marked on the mean axial velocity field for each time period, with $N = 20$ and $\Delta t = 0.4$ s. The symbol $*$ is used if spectra are distinctly and continuously peaked at $m = +1$, and $\triangle$ is used if spectra are distinctly peaked at $m = +1$ but this peak disappears during some of the periods after its first appearance.

quickly disappeared. A vortex pair, i.e. a nearly axisymmetric bubble, was formed at $t = 46.8$ s (figure 20*c* at $t = 46.8$ s) with counter-rotating vortices on each side of the axis. A reverse flow existed between them and two stagnation points bounded the bubble. This near-axisymmetric bubble became asymmetric quickly, then propagated

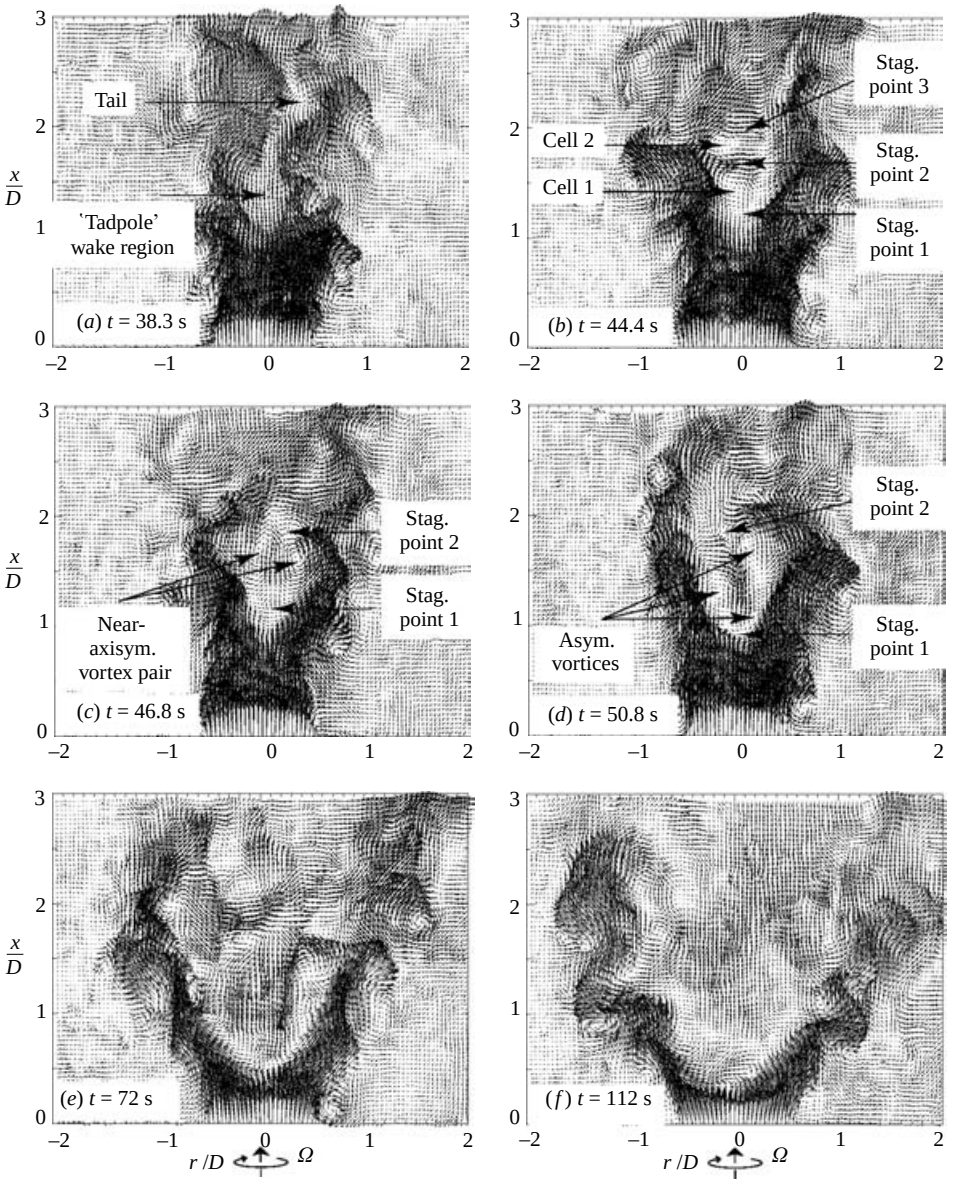

FIGURE 20. Vector images around the vortex breakdown. (*a*) At $t = 38.8$ s, a tadpole-shaped wave region is formed in the vortex core; (*b*) $t = 44.4$ s, two 'one-cell' bubbles are generated and bounded by three stagnation points; (*c*) $t = 46.8$ s, a near-axisymmetric bubble is generated and bounded by two stagnation points; (*d*) $t = 50.8$ s, the bubble becomes asymmetric; (*e*) $t = 72$ s, breakdown stabilizes at $x = 0.5D$ and after that, $m = +1$ takes over the inner shear layer; (*f*) $t = 112$ s, breakdown stabilizes at $x = 0.4D$ and after that, $m = +1$ takes over the outer shear layer and overwhelms the whole flow.

downstream and disappeared. Another axisymmetric bubble formed at $t = 49.2$ s and stayed in the flow for about 1 s. The structure of the breakdown became asymmetric (figure 20*d* at $t = 50.8$ s). Vortices between the reverse region and the spreading jet became spiral and started to propagate downstream. During the transition, as the breakdown structure moved upstream, $t = 48$–64 s (figure 19*g*, *h*), the instability wave

packet $m = +1$ did not expand, but stayed around the axis just above and downstream of the first stagnation point. When breakdown moved further upstream, the reverse flow became wider (figure 19*i* at $t = 64$–72 s). The instability wave $m = +1$ became weak along the axis and in the reverse flow, but grew quickly in the inner shear layer. After $t = 72$ s, the bubble found its stable position at $x = 0.5D$ (figure 20*e* at $t = 72$ s), oscillating with a small amplitude. The helical mode $m = +1$ took over the inner shear layer and gave the breakdown structure a spiral shape (figure 19*j*–*l* at $t = 72$–96 s). The second stagnation point moved downstream to the fully turbulent region and became unsteady. A small packet of the helical wave $m = +1$ appeared at large radii at $x = D$ during the period $t = 64$–72 s, but did not grow at first (figure 19*i*–*l* at $t = 64$–96 s). After $t = 96$ s, instability waves $m = +1$ quickly grew in the outer shear layer and overwhelmed the whole flow after $t = 112$ s (figure 19*m*–*o* at $t = 96$–120 s). As the helical wave grew in the outer shear layer, the breakdown structure grew slightly and stabilized at $x = 0.4D$. The reverse flow grew and covered a larger area. The fully turbulent region moved further downstream together with the second stagnation point, and finally disappeared from the observation frame (figure 20*f* at $t = 112$ s).

In conclusion, the instability wave $m = +1$ was initiated in a small region, which formed in the vortex core and at the axial location of a local wake-like flow and where vortex breakdown would occur a short time later. The wave packet with $m = +1$, which was located around the axis in the head of the wake region before breakdown, or just above and underneath the stagnation point shortly after breakdown, grew only slowly until the breakdown structure moved upstream, amplified in size and stabilized. After that, the helical wave $m = +1$ grew rapidly in the inner shear layer and gave the breakdown structure a spiral shape. Many authors have called this flow type a 'spiral breakdown' or 'single-helix', but it really seems to be due to the instability of a nominally axisymmetric flow. The instability wave $m = +1$ grew and expanded quickly into the outer shear layer. Then the helical mode $m = +1$ overwhelmed the whole flow and became a globally unstable/self-excited oscillation. The wake region in the neighbourhood of the stagnation point served as the wave maker and imposed its frequency on the whole flow.

As one possible explanation for these observations, the authors suggest that the wake region around the axis of the jet became absolutely unstable (AU) during the period $t = 32$–40 s, since instability $m = +1$ was initiated there and was not convected away (figure 19*e*). This AU region expanded slightly as breakdown occurred and moved upstream during the period $t = 40$–56 s (figure 19*f*, *g*). It is possible that this AU region was not large enough for $m = +1$ to be self-excited, and the flow was still marginally globally stable. When the bubble moved further upstream and grew larger during the period $t = 48$–56 s, the AU region expanded even more (figure 19*g*), and the flow possibly became globally unstable thereafter. The oscillation $m = +1$ became self-excited, grew exponentially, dominated the inner shear layer and gave the bubble a spiral shape (figure 19*i*). Only when the spiral $m = +1$ had developed fully in the inner shear layer, was the oscillation excited in the outer shear layer where it then grew exponentially. After that they rotated together and dominated the whole flow (figure 19*m*–*o*).

It should be noted that the initiation and expansion of the wave packet $m = +1$, as well as the growth rate of $m = +1$ calculated at the point $x = 0.25D$ and $r = 0.45D$, i.e. $\ln psd = 0.071t + \text{constant}$, may be an under-estimate. The inner shear layer became spiral at $t = 50.8$ s (figure 20*d*). However, the flow was still developing with the breakdown structure growing in amplitude and moving upstream. The unsteadiness of the flow before the bubble was fully developed and stabilized, as well as the highly

turbulent status of the shear layers before the mode $m=+1$ was self-excited, could delay the appearance and under-predict the amplitude of the distinct peak for mode $m=+1$ in the power spectral distribution.

6. Conclusions and discussion

6.1. *Conclusions*

The competing roles of K–H instability and centrifugal instability have been studied in the present experimental investigation. K–H instability in the axial shear layer, leading to vortex ring formation, dominated non-swirling and weakly swirling jets for $0 \leqslant S < S_{c1}$. After the introduction of rotation to the free jet, the combined axial and azimuthal shear layers became unstable. Co-rotating counter-winding helical waves were produced but they remained as a secondary instability for small swirl numbers. The main instability consisted of vortex rings that maintained their axisymmetry upstream, and became tilted downstream. For strongly swirling jets before breakdown, i.e. $S_{c1} < S < S_{c2}$, helical waves broke the axisymmetry of the flow from the spatial origin and replaced vortex rings to become the main vortex structure. The most unstable modes were $m=+2$ and $+3$. The presence of many weak helical waves and random turbulence made these vortex spirals irregular and disorganized. After vortex breakdown, small-scale turbulence was suppressed and the large-scale helical structures became regular and clearly visible. When vortex breakdown reached its steady state, strong helical waves $m=+1$ and $+2$ coexisted (figure 7), with $m=+1$ having the largest amplitude. The helical modes co-rotated with the jet with a phase speed which was the same as the rotation rate of the nozzle exit, while their inclination, or the sense of winding, was in the direction opposite to that of the mean swirl. The winding direction of these helical modes, both in the centrifugally unstable outer (jet) shear layer and in the centrifugally stable co-rotating inner (wake) shear layer, were aligned with local helical vortex lines of the basic flow. The spirals in both the inner and outer shear layers had the same oscillation frequency and propagation speed and were paired together. In all cases the instability had the characteristics of a helical K–H instability and not a centrifugally dominated one. This point is discussed in more detail in § 6.2.

At several places in the present paper, where it seemed appropriate, allusion has been made to concepts of AI/CI, globally excited instability, etc. A number of experiments have been performed to try to determine whether or not such concepts hold for the present flow. While such concepts are very difficult to prove unambiguously, four different pieces of experimental evidence suggest that, for strongly swirling jets, two global modes, $m=+2$ before vortex breakdown and $m=+1$ after breakdown, become self-excited, a behaviour identified as a super-critical Hopf bifurcation. These four pieces of experimental evidence are: (i) the amplitude of oscillation has very distinct peaks at the specified frequency/mode number $m=+1$ and $+2$; (ii) the amplitude of oscillation is proportional to $(S-S_{k1,2})^{1/2}$, where $S_{k1}=0.62$ for $m=+2$, and $S_{k2}=0.87$ for $m=+1$ (these criteria may be slightly under-estimated and it is likely that the real S_{k2} coincides with the critical swirl number for vortex breakdown, $S_{c2}=0.95$); (iii) the amplitude of the oscillation is insensitive to low-level external forcing for modes $m=+1$ and $+2$ above the corresponding critical swirl number, while the amplitude is linearly dependent on the low-level external forcing for these modes under these critical values; (iv) a spectral study of the impulse response as the swirl number is suddenly increased from around the critical value S_{c2} to above it, e.g. from $S=0.9$ to 1.13, shows the immediate damping of the mode $m=+2$ after the impulse

and the exponential growth of the mode $m=+1$ when breakdown stabilizes at a certain axial location. The onset of the unstable global mode $m=+1$ is probably related to the existence of a certain region of local absolute instability (AI) located in the wake region in the neighbourhood of the stagnation point/region.

6.2. *Discussion*

An attempt is made here to compare the present experimental results to some of the existing theories and experiments.

The phase speed of each unstable helical wave observed in the present experiments is the same as the rotation rate of the nozzle, both in direction and absolute value, both before and after breakdown. It should be noted that the rotation rate of the vortex core of the inlet flow is calculated to be exactly the same as that of the nozzle (figure 9*a*). This phenomenon was first found by observation of the vertical and horizontal slices (figures 3 and 4) of the flow. It was then confirmed in the power spectral study, in which the spectral peak was very clearly at some multiple of the rotation rate of the nozzle, which was predicted as the most unstable mode from earlier analogue observation. Support was found in two recent experimental papers. In an investigation of a confined swirling flow by Kurosaka *et al.* (2003), an axisymmetric vortex breakdown bubble was most affected and transformed to a co-rotating spiral vortex breakdown structure with $m=+1$, shortly after the introduction of forcing with $m=+1$ and in a frequency range that corresponded to a rotation rate almost equal to that of the vortex core of the inlet flow. The second supporting instability study by Gallaire, Rott & Chomaz (2003) used the same swirling free jet as Billant *et al.* (1998) and Loiseleux *et al.* (2000). In these earlier papers by this group, the natural rotation rate of the most unstable helical waves was found to be 1/3 smaller than that of the vortex core of the inlet flow, but in this latest paper, they corrected the ratio 1/3 to 1/10. Assuming that this newly reported value of the ratio is more accurate and reliable, the forcing phase speed, which was used by them to achieve the most amplified helical waves, with $|m|=2$ and 3 before breakdown, is one order of magnitude, 10 times, greater than the natural value of 1/10, i.e. the same as the rotation rate of the inlet vortex core. This agrees well with the present observation. Furthermore, using the stability calculations of Gallaire & Chomaz (2003*b*), we find agreement that the calculated phase speed of their $m=+1$ and $+2$ modes in a temporal stability study is close to the rotation rate of the vortex core at the inlet. Of course, the velocity profiles used in the above experimental and numerical investigations are somewhat different from ours and the comparison is only suggestive and not absolute.

A necessary condition was derived by Howard & Gupta (1962) for the temporal instability of vortex flows. This condition is a function of:

$$G=\frac{m}{kr}, \quad C_x=\frac{r}{w}\frac{\mathrm{d}u}{\mathrm{d}r} \quad \text{and} \quad C_\theta=\frac{r}{w}\frac{\mathrm{d}w}{\mathrm{d}r}$$

$$K=(1+C_\theta)-GC_x-\tfrac{1}{8}[C_x+G(C_\theta-1)]^2<0 \tag{6.1}$$

where (u, w) and $(\omega_x, \omega_\theta)$ are velocity and vorticity in the axial and azimuthal directions (x, θ). According to Rayleigh's criterion, the flow is centrifugally unstable if $1+C_\theta<0$. At the same time, Ludwieg (1960, 1961, 1964) found a sufficient condition but his theory was limited to vortex flows in a small gap. Leibovich & Stewartson (1983) derived a sufficient condition applicable to columnar vortex jets in unbounded

domains,

$$w\frac{\mathrm{d}(w/r)}{\mathrm{d}r}\left[\frac{\mathrm{d}(w/r)}{\mathrm{d}r}\frac{\mathrm{d}wr}{\mathrm{d}r}+\left(\frac{\mathrm{d}u}{\mathrm{d}r}\right)^2\right]<0. \tag{6.2}$$

According to this criterion, the unstable modes are aligned with a helix angle which equals

$$\theta_1=\tan^{-1}(\mathrm{d}w/\mathrm{d}r-w/r)/(\mathrm{d}u/\mathrm{d}r)=\tan^{-1}(C_\theta-1)/C_x$$

whereas the vortex lines are aligned along

$$\theta_2=\tan^{-1}\omega_x/\omega_\theta=\tan^{-1}-(\mathrm{d}w/\mathrm{d}r+w/r)/(\mathrm{d}u/\mathrm{d}r)=\tan^{-1}[-(1+C_\theta)/C_x].$$

After applying to local velocity profiles available from the present experiments, these two angles as well as the helix angle

$$\theta_3=\tan^{-1}(-m/kr)=\tan^{-1}(-G)$$

corresponding to Howard & Gupta's criterion at minimum value of K, were calculated as a function of radius for strong swirling jets before breakdown and after breakdown (figure 21a, b). The helical waves and the mean vortex are co-winding if the angle has a positive value and are counter-winding if negative. The inlet region for flow before breakdown and the wake region around the stagnation point after breakdown are the most likely locations for instability initiation (also noticed by Gallaire & Chomaz 2003b) and they were chosen for further study. The results were calculated from the mean axial velocity at $S=0.71$ and 1.07 (figure 10) of flow B and from the mean azimuthal velocity at $S=0.78$ and 0.98 (figure 9) of flow A. For comparison, instant images with vectors and vorticity contours on a vertical slice are shown in figure 21(c) at $S=0.71$ and 1.07 for flow B, and the approximate locations and angles, $\theta_4=\tan^{-1}2\delta x/\pi\delta r$, of these counter-winding spirals are marked. As shown in figure 21(b, c), the unstable waves proposed by Leibovich & Stewartson's criterion, θ_1, are co-winding, whereas both vortex lines and helical waves observed in the present experiments, θ_2 and θ_4, as well as the helix corresponding to Howard & Gupta's criterion at min(K), θ_3, are counter-winding. One interesting result is that the helix angle calculated from Howard & Gupta's criterion at min(K) agrees very well with the present experiments, e.g. $\theta_3=-28^\circ$ or -30° whereas $\theta_4=-22^\circ$ at $x=0^\circ$ with $S=0.71$–0.78, and $\theta_3=-13^\circ$ or -15° while $\theta_4=-7^\circ$ or -9° at $x=0.5D$ for $S=1.07$–0.98. As pointed out by a referee there is no logical basis for the most unstable mode to correspond with the minimum of K, and the present authors are in full agreement with this statement. The points are included in figure 21 as a challenge to the community of theoreticians to determine if such a result can be rigorously justified or is simply an interesting coincidence. It should also be noted that even though the helical waves estimated on instantaneous images have the same winding direction as the mean vortex lines, their absolute angle, $|\theta_4|=22^\circ$ at $S=0.71$ and 7° or 9° at $S=1.07$, is obviously smaller than that of the latter which are $|\theta_2|=40^\circ$–50° at $S=0.71$–0.78 and 20°–25° at $S=1.07$–0.98 (figure 21b, c).

Agreement with the present experiments can be found in calculations by Martin & Meiburg (1994), Lim & Redekopp (1998), Loiseleux *et al.* (2000), Gallaire & Chomaz (2003a) and Ruith *et al.* (2003) for cases of centrifugally unstable jets and centrifugally stable wakes at the inlet, in which the axial and azimuthal shear layers coincide, and to some extent the theory by Gallaire & Chomaz (2003b). Co-rotating counter-winding helical waves which had the same winding direction as the mean vortex lines in shear layers between the jet or wake and its surroundings, were found to

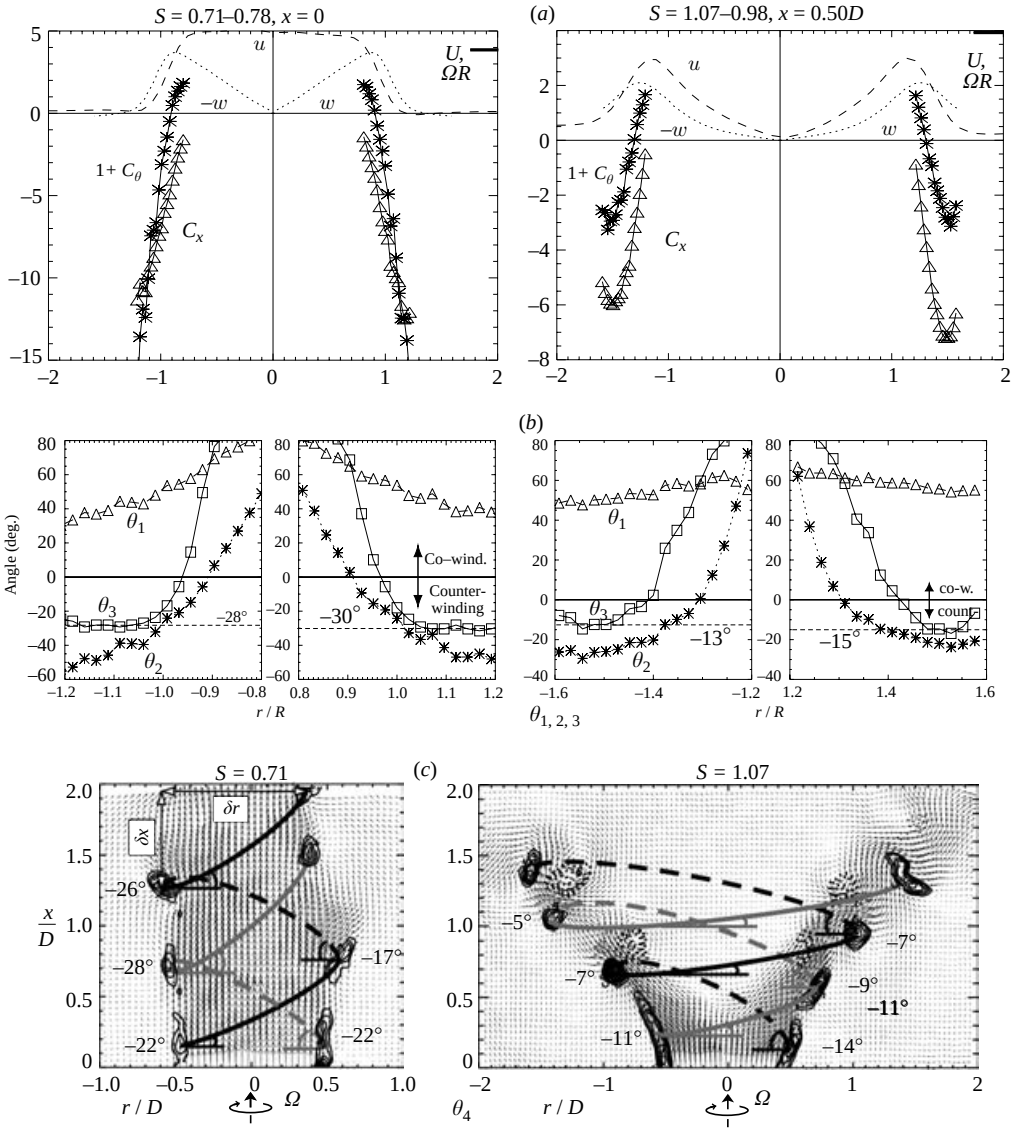

FIGURE 21. The angle of the mean vortex lines and the unstable helical waves within the outer shear layer at the inlet for a strong swirling jet before breakdown and around the stagnation point for flow after breakdown. (*a*) Velocity profiles (u, w) and vorticity constants $(1+C_\theta, C_x)$. (*b*) The angle of the unstable wave $\theta_1 = \tan^{-1}(C_\theta - 1)/C_x$ proposed by Leibovich & Stewartson (1983), of the mean vortex $\theta_2 = \tan^{-1} -(1+C_\theta)/C_x{}^\circ$ and of the helical wave $\theta_3 = \tan^{-1}(-G)$ corresponding to minimum K proposed by Howard & Gupta (1962) when applied to the present base flow. (*c*) Spatial evolution of the vortex spirals, $m = +2$ at $S = 0.71$, and $m = +1$, $+2$ at $S = 1.07$, $Re = 1000$. The angle of these counter-winding helical waves, $\theta_4 = \tan^{-1} 2\delta x/\pi\delta r$, is noted. At $S = 1.07$, the black spiral is the stronger mode $m = +1$ which has a strong companion vortex on the inner shear layer. Note the change in the scale of r between (a, b), r/R, and (c), r/D.

be the most unstable. Similarily the theory of Loiseleux *et al.* (2000) agrees with present experimental observations for non-swirling and weakly swirling jets, in which the axial shear-layer instability leads to vortex rings, $m = 0$, dominating the flow. Experimentally, counter-rotating and co-winding helical waves were found before

breakdown by the LadHyX group, Billant *et al.* (1998) and Loiseleux & Chomaz (2003) based on observations of a swirling free jet with subtly different inlet velocity profiles from the present ones (see comments in § 1). The former found $m = -2$ for moderate Reynolds numbers and $m = -3$ for larger Reynolds numbers before breakdown, and the latter authors reported that the most unstable helical wavenumber m ranged from -7 to -1 as S increased. Helical waves with high phase speed became the most unstable at large swirl rates just before the onset of breakdown. Gallaire & Chomaz (2003*b*) applied linear stability analysis to inlet velocity profiles that modelled those of Billant *et al.* (1998), and found a counter-rotating co-winding mode, $m = -2$, becoming AU for centrifugally unstable jets. This mode had a phase speed 1/3.3 times the rotation rate of the inlet vortex core at the critical swirl number where it became AU. At a similar value of swirl rate, Loiseleux & Chomaz (2003) observed the double-helix $m = -2$ counter-rotating with the jet with a phase speed 1/3 times the measured rotation rate measured at $x = 22$ mm. As one possibility, it seems that due to the subtle differences in the location of the maxima of the azimuthal and axial shear layers the LadHyX group generated co-winding waves that were driven by centrifugal instability, since the maximum azimuthal shear was at a radial location where the axial shear was weaker. On the contrary our counter-winding waves, with both shear layers coincident, were more aligned with the mean vortex lines. The Rayleigh centrifugal instability is not relevant for these counter-winding helical waves but, instead, a combination or competition of the K–H instability and the generalized centrifugal instability of Ludwieg (1960, 1961, 1964) and Leibovich & Stewartson (1983). It is possible that the nature of the instability depends very critically on the relative thicknesses and radial displacements of the two shear layers (L. G. Redekopp, private communication). It should be noted that in the temporal stability study by Gallaire & Chomaz (2003*b*) of the Billant *et al.* (1998) velocity profiles, co-rotating counter-winding modes $m = +1$, $+2$ and $+3$ were unstable but with lower growth rate than those of the modes $m \leqslant 0$. For large swirling rates, the phase speed of $m = +1$ or $+2$, at its most unstable axial wavenumber, was close to the rotation rate of the inlet flow, agreeing with the observations of the present experiments. However, since m-positive waves were found by them to have smaller growth rates in the temporal stability study, they were excluded from further study of the absolute/convective nature of the instability.

Unfortunately, no theoretical or computational proof has been given for the existence of locally absolutely unstable helical waves or globally unstable modes applied to basic velocity profiles exactly the same as those of the present inlet flow. Thus, interpretations of a local/global and convective/absolute instability nature have been provided as suggestions only, especially for flows before breakdown. A spatially developing numerical model of swirling jets has been recently studied by Ruith *et al.* (2003), and the spiral type of breakdown was found to have a similar but not identical spatial and temporal evolution to that observed in present experiments. There are several points to be noted about that computational work. First of all, velocity profiles of the inflow, i.e. at the spatial origin $x = 0$, were unchanged by the presence of breakdown in contrast to the present work. Secondly, the shear layer of their model was centrifugally stable at the spatial origin $x = 0$, and centrifugally unstable profiles only evolved around the breakdown bubble at large swirl number. Thus, unfortunately, a general study of centrifugally unstable swirling jets was excluded. Nonetheless interesting comparisons between that work and the present experiments remain. In particular an $m = +1$ mode evolved initially somewhat downstream of the breakdown bubble but it very rapidly spread upstream to encompass, and distort, the

breakdown bubble itself. In this regard the final flow field was virtually identical to that found in the present experiments. By showing that the wake flow after breakdown was absolutely unstable they strengthen the assertion that the present flow was also absolutely unstable and that it was likely to be a nonlinear global mode. Further support for this point of view comes from recent work at LadHyX by Ruith *et al.* (2004) which suggests that the observations of an unstable region downstream of the breakdown region in Ruith *et al.* (2003) can be interpreted as being the result of the breaking of the symmetry of the vortex breakdown to a nonlinear steep global mode, in the sense of Pier & Huerre (2001), in the wake of the breakdown bubble. This further implies that the observations of rapid spiral wave growth in the same region, in the experiments presented in § 5.4.3, has a similar explanation.

This work was supported by the National Science Foundation under Grant No. CTS-9523291. Discussions with Professors L. G. Redekopp, F. K. Browand, P. Huerre and J.-M. Chomaz and Dr F. Gallaire, as well as the technical help of Professors G. R. Spedding and A. M. Fincham are gratefully acknowledged. The authors also wish to thank the reviewers for their helpful suggestions for improvement of an earlier draft. Further experimental results are given in Liang (2003) and Liang & Maxworthy (2005).

REFERENCES

Benjamin, T. B. 1962 Theory of the vortex breakdown phenomenon. *J. Fluid Mech.* **14**, 593.

Billant, P., Chomaz, J. M. & Huerre P. 1998 Experimental study of vortex breakdown in swirling jet. *J. Fluid Mech.* **376**, 183.

Browand, F. K. & Laufer, J. 1977 The role of large-scale structures in the initial development of circular jets. *Turbulence in Liquids, Proc. 4th Symp. on Turbulence in Liquids, University of Missouri–Rolla, Sept. 1975*, pp. 333–344. Science Press.

Brown, G. & Lopez, J. 1990 Axisymmetric vortex breakdown Part 2. Physical mechanisms. *J. Fluid Mech.* **221**, 553.

Chigier, N. A. & Chervinsky, M. R. 1967 Experimental investigation of swirling vortex motion in jets. *Trans. ASME: J. Appl. Mech.* **34**, 443.

Chomaz, J.-M., Huerre, P. & Redekopp, L. 1988 Bifurcations to local and global modes in spatially developing flows. *Phys. Rev. Lett.* **60**, 25.

Delbende, I., Chomaz, J.-M. & Huerre, P. 1998 Absolute/convective instability in the Bachelor vortex: a numerical study of the linear impulse response. *J. Fluid Mech.* **355**, 229.

Escudier, M. 1987 Confined vortices in flow machinery. *Annu. Rev. Fluid. Mech.* **19**, 27.

Escudier, M., Bornstein, J. & Maxworthy, T. 1982 The dynamics of confined vortices. *Proc. R. Soc. Lond.* A **335 19**, 27.

Fincham, A. M. & Spedding, G. R. 1997 Low cost, high resolution DPIV for measurement of turbulent fluid flow. *Exps. Fluids* **23**, 449.

Fuchs, V., Ko, K. & Bers, A. 1981 Theory of mode-conversion in weakly inhomogeneous plasma. *Phys. Fluids* **24**, 1251.

Gallaire, F. & Chomaz, J.-M. 2003*a* Instability mechanisms in swirling flows. *Phys. Fluids* **15**, 2622.

Gallaire, F. & Chomaz, J.-M. 2003*b* Mode selection in swirling jet experiments: a linear stability analysis. *J. Fluid Mech.* **494**, 223.

Gallaire, F., Rott, S. & Chomaz, J.-M. 2003 Experimental study of a free and forced swirling jet. Submitted to *J. Fluid Mech.*

Gupta, A. K., Lilley, D. G. & Syred, N. 1984 Swirl flows. *Kent Engl: Abacus* 475.

Hall, M. G. 1972 Vortex breakdown. *Annu. Rev. Fluid Mech.* **4**, 195.

Harvey, J. K. 1962 Some observations of the vortex breakdown phenomenon. *J. Fluid Mech.* **14**, 585.

Howard, L. N. & Gupta, A. S. 1962 On the hydrodynamic and hydromagnatic stability of swirling flows. *J. Fluid Mech.* **14**, 463.

Huerre, P. 2001 Open shear flow instabilities. In *Perspectives in Fluid Dynamics, A Collective Introduction to Current Research.* Cambridge University Press.

Huerre, P. & Monkewitz, P. 1990 Local and global instabilities in spatially developing flows. *Annu. Rev. Fluid. Mech.* **22**, 473.

Koch, W. 1985 Local instability characteristics and frequency determination of self-excited wake flows. *J. Sound Vib.* **99**, 53.

Kribus, A. & Leibovich, S. 1994 Instability of strong nonlinear waves in vortex flows. *J. Fluid Mech.* **269**, 247.

Kurosaka, M., Kikuchi, M., Hirao, K., Yuge, T. & Inoue, H. 2003 Interchangeability of vortex breakdown types. *Exps. Fluids* **34**, 77.

Lambourne, N. C. & Bryer, D. W. 1961 The bursting of leading-edge vortices: some observation and discussion of the phenomenon. *Aero. Res. Counc. R&M* **36**, 3282.

Landau, L. D. & Lifshitz, E. M. 1959 *Fluid Mechanics.* Pergamon.

Leibovich, S. 1970 Weakly nonlinear waves in rotating fluids. *J. Fluid Mech.* **42**, 803.

Leibovich, S. 1978 The structure of vortex breakdown. *Annu. Rev. Fluid Mech.* **10**, 221.

Leibovich, S. 1983 Vortex stability and breakdown: survey and extension. *AIAA J.* **22**, 1192.

Leibovich, S. & Ma, H. Y. 1983 Soliton propagation on vortex cores and the Hasimoto soliton. *Phys. Fluids* **26**, 3173.

Leibovich, S. & Randall, J. D. 1973 Amplification and decay of long nonlinear waves. *J. Fluid Mech.* **53**, 481.

Leibovich, S. & Stewartson, K. 1983 A sufficient condition for the instability of columnar vortices. *J. Fluid Mech.* **126**, 335.

Liang, H. 2003 Experimental investigations of swirling jets. PhD thesis, Univ. Southern California.

Liang, H. & Maxworthy, T. 2005 Vortex breakdown and mode selection of swirling jets in stationary or rotating surroundings. (In preparation)

Lim, D. & Redekopp, L. 1998 Absolute instability conditions for variable density, swirling jet flows. *Eur. J. Mech.* B/*Fluids* **17**, 165.

Lingwood, R. J. 1995 Absolute instability of the boundary layer on a rotating disk. *J. Fluid Mech.* **299**, 17.

Lingwood, R. J. 1996 An experimental study of absolute instability of the rotating-disk boundary-layer flow. *J. Fluid Mech.* **314**, 373.

Loiseleux, T., Chomaz, J.-M. & Huerre, P. 1998 The effect of swirl on jets and wakes: linear instability of the Rankine vortex with axial flow. *Phys. Fluids* **10**, 1120.

Loiseleux, T. & Chomaz, J.-M. 2003 Breaking of rotational symmetry in a swirling jet experiment. *Phys. Fluids* **15**, 511.

Loiseleux, T., Delbende, I. & Huerre, P. 2000 Absolute and convective instabilities of a swirling jet/wake shear layer. *Phys. Fluids* **12**, 375.

Ludweig, H. 1960 Stabilität der Strömung ineinem zylindrischen Ringraum, *Z. Flugwiss.* **8**, 135.

Ludweig, H. 1961 Erganzungzu der Arbeit: "Stabilität der Strömung in einem zylindrischen Ringraum", *Z. Flugwiss.* **9**, 361.

Ludweig, H. 1964 Experimentelle Nach prüfung der Stäbilitätstheorien für reibungsfreie Strömung mit Schraublinienförmigen Strömlinien. *Z. Flugwiss.* **12**, 304.

Mahesh, K. 1996 A model for the onset of breakdown in an axisymmetric compressible vortex. *Phys. Fluids* **8**, 3338.

Martin, J. & Meiburg, E. 1994 On the stability of the swirling jet shear layer. *Phys. Fluids* **6**, 424.

Mathis, C., Provansal, M. & Boyer, L. 1984 The *Bénárd–Von Kármán* instability: an experimental study near the threshold. *J. Phys. Lett. (Paris)* **45**, 483.

Maxworthy, T., Hopfinger, E. J. & Redekopp, L. G. 1985 Wave motions on vortex cores. *J. Fluid Mech.* **151**, 141.

Monkewitz, P. A. 1988 The absolute and convective nature of instability in two-dimensional wakes at low Reynolds numbers. *Phys. Fluids* **31**, 999.

Monkewitz, P. A., Bechert, D. W., Barsikow, B. & Lehmann, B. 1990 Self-excited oscillations and mixing in a heated round jet. *J. Fluid Mech.* **213**, 611.

Olendraru, C. & Sellier, A. 2002 Absolute/convective instability of the Batchelor Vortex in the viscous case. *J. Fluid Mech.* **459**, 371.

Olendraru, C., Sellier, A., Rossi, M. & Huerre, P. 1999 Inviscid instability of the Batchelor vortex: absolute/convective transition and spatial branches. *Phys. Fluids* **11**, 1805.

Panda, J. & McLaughlin, D. K. 1994 Experiments on the instabilities of a swirling jet. *Phys. Fluid* **6**, 263.

Pier, B. & Huerre, P. 2001 Nonlinear self-sustained structures and fronts in spatially developing flows. *J. Fluid Mech.* **435**, 145.

Pier, B., Huerre, P. & Chomaz, J.-M. 2001 Bifurcation to fully nonlinear synchronized structure in slowly varying media. *Physica* D **148**, 49.

Randall, J. D. & Leibovich, S. 1973 The critical state: a trapped wave model of vortex breakdown. *J. Fluid Mech.* **53**, 495.

Ruith, M. R., Chen, P., Meiburg, E. & Maxworthy, T. 2003 Three-dimentional vortex breakdown in swirling jets and wakes: direct numerical simulation. *J. Fluid Mech.* **486**, 331–378.

Ruith, M. R., Gallaire, F., Chomaz, J-M., Huerre, P. & Meiburg, E. 2004 Spiral vortex breakdown as a global mode. *Presented at the 21st Intl Congr. on Theoretical and Applied Mechanics, Warsaw, Poland, August 2004.* IUTAM.

Ruith, M. R. & Meiburg, E. 2001 Direct numerical simulation of spatially developing, three-dimensional swirling jets. *Bull. APS Annual Meeting DFD01 Session: AN.007.*

Sarpkaya, T. 1971 On stationary and travelling vortex breakdown. *J. Fluid Mech.* **45**, 545.

Spall, R. E., Gatski, T. B. & Grosch, C. E. 1987 A criterion for vortex breakdown. *Phys. Fluids* **30**, 3434.

Squire, H. B. 1962 Analysis of the vortex breakdown phenomenon. In *Miszellaneen der Angewandten Mechanik*, p. 306. Akademie-Verlag, Berlin.

Strykowski, P. J. 1986 The control of absolutely and convectively unstable shear layers. PhD thesis, Yale University.

Strykowski, P. J. & Niccun, D. L. 1991 The stability of counter-current mixing layers in circular jets. *J. Fluid Mech.* **227**, 309.

Wang, S. & Rusak, Z. 1997 The dynamics of a swirling flow in a pipe and transition to axisymmetric vortex breakdown. *J. Fluid Mech.* **340**, 177.

Yin, X. Y., Sun, D. J., Wei, M. J. & Wu, J. Z. 2000 Absolute and convective instability character of slender viscous vortices. *Phys. Fluids* **12**, 1062.